Global and Interregion Characterization of Subduction Interface Earthquakes Derived From Source Time Functions Properties

Agnès. Chounet, Martin Vallée

Check for updates

RESEARCH ARTICLE

Key Points:
- Dip-slip earthquakes are characterized using the SCARDEC global database of source time functions
- Subduction interface earthquakes have systematically lower stress drops than other earthquakes
- A positive correlation is found between subduction earthquakes impulsivity and interface coupling

Supporting Information:
- Supporting Information S1

Correspondence to:
A. Chounet,
chounet@ipgp.fr

Global and Interregion Characterization of Subduction Interface Earthquakes Derived From Source Time Functions Properties

Agnès Chounet[1,2] iD **and Martin Vallée[1]** iD

[1]Institut de Physique du Globe de Paris, Sorbonne Paris Cité, Université Paris Diderot, CNRS, Paris, France, [2]Now at Institut de Physique du Globe de Strasbourg, Université de Strasbourg, CNRS, Strasbourg, France

Abstract Source time functions (STFs) describe how the seismic moment rate is released with time, and carry information on integral rupture properties, such as static stress drop and radiated energy. In this study, we systematically analyze a set of 1,433 STFs extracted from the SCARDEC method (Vallée and Douet, 2016, https://doi.org/10.1016/j.pepi.2016.05.012), containing the $M_w \geq 5.6$, shallow ($z \leq 70$ km) earthquakes with dip-slip mechanism that occurred between 1992 and 2014. At the global scale, STFs properties indicate scale invariance of stress drop and scaled radiated energy with magnitude. In a second step, these source parameters are investigated in light of the tectonic context of the earthquakes: in agreement with other approaches, we observe that subduction interface earthquakes have lower stress drop and scaled radiated energy relative to all other earthquakes (e.g., crustal earthquakes). Finally, a focus on subduction interface earthquakes (approximately 800 earthquakes) is done by considering 18 regional segments of subduction zones. We find that these segments do not have the same signature in terms of macroscopic rupture properties, which means that large-scale plate convergence and mechanical properties influence rupture behavior. In a given segment, local heterogeneities of stress drop or radiated energy can be associated with local features of the subduction zone: in particular, we find that low coupled zones generate earthquakes with low stress drop and scaled radiated energy. This last feature, also observed at a larger scale, suggests a positive correlation between coupling and stress drop.

1. Introduction

The rapidly increasing number of earthquakes well recorded by modern seismometers offers the possibility to look for generic properties of the earthquake process, both at the global and the regional scales. In this respect, the richest information theoretically comes from detailed space-time slip inversions, using, for example, compilations made in the frame of the SRCMOD project (http://equake-rc.info/srcmod/; Mai & Thingbaijam, 2014) or systematic teleseismic approaches (Melgar & Hayes, 2017; Ye et al., 2016). However, the number of earthquakes that can be accurately described as extended sources remains moderate, and the use of compilations based on different approaches and data sets raises some concerns about the source parameters that can safely be compared between models. Based on these limitations, seismologists may prefer simpler observables that can be robustly determined for a large number of earthquakes and with similar techniques. The most classical one is the corner frequency f_c of the seismic spectrum, which can be related to the stress drop $\Delta\sigma$ when assuming a simple source model with constant rupture velocity (e.g., Brune, 1970; Madariaga, 1976). Systematic analyses of the corner frequency have been done both at the local scale (Prejean & Ellsworth, 2001; Uchide et al., 2014, for instance) and at the global scale (e.g., Allmann & Shearer, 2009, and more recently Denolle & Shearer, 2016).

Another exhaustive way to have access to the stress drop is through the earthquakes moment rate functions, also referred to as source time functions (STF). STFs (Bilek et al., 2004; El Hariri et al., 2013; Houston, 2001; Tanioka & Ruff, 1997) describe the time history of moment rate release and thus give a direct access to the source duration and peak moment rate, which can be related, similarly to corner frequency, to the static stress drop (e.g., Bilek et al., 2004; Houston, 2001). Compared to corner frequency measurements, STFs present the advantage of providing access to the full spectrum of the seismic source. This is important to account for complex earthquakes that cannot be simply described with a unique corner frequency, and this also offers the possibility to estimate the seismic energy E_R radiated by the rupture (e.g., Bilek et al., 2004; Vassiliou &

Kanamori, 1982). The radiated energy normalized to seismic moment M_0, or equivalently, the apparent stress ($\sigma_a = \mu \frac{Er}{Mo}$, with μ the medium rigidity), quantifies the radiative character of a rupture (Abercrombie & Rice, 2005).

As a consequence of the teleseismic wavefield properties, STFs are closely related to the real broadband waveforms (basically through a deconvolution from the Green function of the medium) and as such provide robust information on the source process. The SCARDEC method (Vallée & Douet, 2016; Vallée et al., 2011) takes advantage of this configuration to extract, from the teleseismic body waves, a homogeneous database of several thousands of STFs for earthquakes with $M_w \geq 5.8$ (http://scardec.projects.sismo.ipgp.fr). SCARDEC method further provides, jointly with the STFs, determinations of the focal mechanism, depth, and moment magnitude which have been shown to be consistent with GCMT (Ekström et al., 2012; Vallée & Douet, 2016). This database has already been exploited to show that the stress drop increase with depth follows the medium rigidity increase, implying a constant strain drop $\Delta\epsilon$ between 0- and 650-km depth (Vallée, 2013). It has also been used to explore the global stress drop variability for shallow earthquakes, which is found to be reduced relative to other global databases (Courboulex et al., 2016). The epistemic variability is hence reduced, and the observed variability reflects more closely the actual diversity of rupture processes.

In this study, we propose to characterize this variability, with a specific focus on subduction earthquakes. Subduction zones are very active and with dominantly dip-slip mechanisms, easier to analyze with teleseismic body wave STFs than strike-slip mechanisms. In a range of depths between Earth surface and about 70 km, they mostly host seismic events that occur on the plate interface, with a thrust mechanism, and classically referred to as subduction interface earthquakes. This vast class of earthquakes has some seismic characteristics which can be distinguished from the ones of earthquakes observed in other contexts. Analysis of their corner frequencies (Allmann & Shearer, 2009) or their STFs durations (Courboulex et al., 2016; Houston, 2001) show that they are in average less impulsive than intraplate earthquakes. Consistently, they are also characterized by a lower apparent stress (Choy & Boatwright, 1995). This may explain that crustal earthquakes tend to cause larger damages than subduction earthquakes (Choy & Kirby, 2004).

Besides these global characteristics, subduction interplate seismicity also has its own diversity, firstly related to the depth-dependent properties of the subduction interface. In the very shallow part of the interface, seismicity is sparser, due to the presence of a conditionally stable interface (Lay et al., 2012). Rupture is therefore unlikely to nucleate there, and most of the earthquakes affecting this area initiate at greater depth before propagating toward the surface. As these shallow earthquakes propagate in a hydrated and low rigidity medium, they are expected to have a long duration with respect to their moment magnitude and a strong tsunami potential. It has been indeed observed that shallow and tsunamigenic ruptures are characterized by longer durations and lower radiations, compared to earthquakes occurring in the most seismogenic part of the subduction interface (between 20- and 50-km depth; Bilek & Lay, 1999; Bilek et al., 2004; Convers & Newman, 2011; Duputel et al., 2013). This general scheme is not fully valid for every subduction. In particular, some subductions are found to be almost decoupled in the 20- to 50-km depth interval (e.g., North Peru, Nocquet et al., 2014; Java, Abercrombie et al., 2001; Nicaragua, Correa-Mora et al., 2009), in which case the interplate seismicity tends to be dominated by the occurrence of shallow and tsunamigenic earthquakes. Earthquake properties between subductions also differ in more subtle ways, differences which can originate from the specificities of each subduction in terms of plate convergence velocity, age, and topography of the subducting plate. For instance, the background seismicity and b value of the Gutenberg-Richter law are found to be variable among subduction zones and can be related to the plate convergence properties (Ide, 2013; Nishikawa & Ide, 2014). In this study, we propose to use the SCARDEC STFs database to further explore the characteristics of the earthquakes occurring in subduction contexts. This will be first performed through a global analysis of the whole shallow ($z \leq 70$ km) dip-slip-type seismicity occurring on Earth in order to extract its global behavior, and how subduction interplate earthquakes differ from the general trend. Then, interregion differences among subduction earthquakes will be analyzed and discussed in association with tectonic and mechanical features of plate convergence.

2. Source Properties Extracted From the SCARDEC STF Database
2.1. Catalog of Mean STFs and Earthquakes Classification
2.1.1. Mean STFs From the SCARDEC Database
SCARDEC (Vallée & Douet, 2016; Vallée et al., 2011) is a method that routinely analyzes teleseismic records for moderate to large earthquakes in order to retrieve the earthquake STF, together with seismic moment,
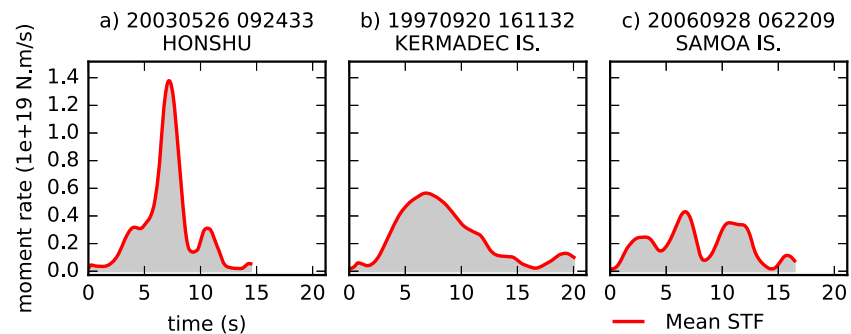
Figure 1. Source time functions (STFs) of three $M_w \simeq 7$ earthquakes. The gray area under the curve corresponds to the seismic moment M_0. (a) STF with a very high peak and short duration. (b, c) STFs with lower peaks and longer durations. Note the difference in complexity between (b) and (c) STFs.

focal mechanism, and focal depth. The analysis, based on a joint deconvolution of the P and SH body waves, retrieves an apparent STF (ASTF) for each phase, at each selected teleseismic broadband station recording the earthquake. Data come from the Federation of Digital Seismograph Networks, with an extensive use of the IRIS/USGS (II or IU) and GEOSCOPE networks. The differences between ASTFs for a given earthquake originate from the spatiotemporal source properties which distort the absolute STF. In order to approximate this absolute STF, a mean STF is computed from the P waves ASTFs, when at least eight P waves ASTFs are available. The procedure first shifts the ASTFs to maximize their correlation then stacks the shifted ASTFs. The final mean STF (referred to as the STF in the following) is obtained after removing the incoherent and low-amplitude features present in the late parts of the stack that can be attributed to nonmodeled propagation effects (Vallée & Douet, 2016). The resulting STF constitutes a good proxy of the absolute moment rate function. The STFs of three M_w 7 earthquakes are represented in Figure 1 and exhibit a large variety of shape in spite of their similar seismic moment.

These variations provide information about the seismic source itself and can also potentially be affected by propagation effects, as a result of the underlying assumptions made about the structure and attenuation in the SCARDEC method. The assumed velocity structure is the IASP91 radial Earth structure (Kennett & Engdahl, 1991), except for the source crustal structure, derived from the 3-D crust model CRUST2 (Bassin et al., 2000; note that the most recent version of SCARDEC database, available online, now considers CRUST1): a linear velocity and density gradient, over a thickness dependent on the CRUST2 Moho depth, is assumed at each source location. Although not accurate to model high-frequency wave propagation in complex contexts such as subduction zones, the smoothness of this assumed structure avoids to map artificial complexities into the STF. STF amplitudes would, however, be biased if the depth-dependent structure is systematically different from the actual depth structure, for example, in subduction contexts. As STFs duration would be comparatively little affected by these structure effects, such a systematic error would result in a bias of the SCARDEC seismic moment as a function of depth. The comparison with GCMT (Ekström et al., 2012; Vallée & Douet, 2016), which uses other wave types and structure description, does not support this hypothesis (Figure S1 of the supporting information), implying that a general bias with depth appears unlikely.

In terms of attenuation, its first-order effects are taken into account in the SCARDEC method. Mantle attenuation is modeled by a frequency-dependent t^* operator (see Vallée & Douet, 2016), which is the same for all earthquakes and all paths (but different between P and SH waves, $t^*(SH) \simeq 4t^*(P)$). The use of the reflectivity method (Müller, 1985) in both the source and receiver sides allows us to take also into account the crustal attenuation of both P and SH waves ($Q_P \simeq 500$ and $Q_S \simeq 200$ in each crustal layer). The point source synthetics are computed with these attenuation corrections, meaning that the SCARDEC STFs, derived from deconvolving the data from these synthetics, are also corrected to the first order from these attenuation effects. At the other side of the spectrum, data and synthetics are always high-pass filtered below the corner frequency of the earthquake (down to 0.003 Hz for very large earthquakes), which means that low frequencies should be well retrieved.

Even if these STFs are in theory fully broadband, it is clear that the way of managing attenuation effects is too simplistic to be exact for each path and that very high frequencies are lost in the STF even if they were present at the source. The effect of the latter point is increased by the fact that we here consider mean STFs

(for robustness purposes), and averaging over ASTFs is destructive for high frequencies. Hence, in spite of the attenuation correction performed in the SCARDEC analysis, a correction still appears required. In the following sections, depending on the metrics considered, a specific correction is thus performed.

2.1.2. STFs Selection and Tectonic Classification

SCARDEC analysis has been applied on the worldwide seismicity from January 1992, and our current study focuses on the time period between January 1992 and July 2014. It provides a catalog of STFs for more than 2,700 earthquakes with magnitude ranging from 5.6 to 9.1. Within this database, STFs of dip-slip earthquakes are more reliable than those of strike-slip earthquakes. For the strike-slip earthquakes, the teleseismic waves come from a region close to the nodal planes, resulting in low-amplitude waves. In addition, in the case of oceanic transform faults earthquakes, the complex structure around the source, not taken into account by the Green function, is mapped into the source term, leading to abnormally complex (e.g., artificially rough) and long STFs. On the other hand, the teleseismic P wave radiations for dip-slip earthquakes are strong and hence provide more reliable STFs. In order to accurately measure source parameters from the functions, we prefer to discard the less reliable ones, that is, the strike-slip earthquakes STFs, and focus on the dip-slip ruptures (including oblique mechanisms). This selection is based on the focal mechanism rake angle, λ, as defined in the Aki-Richards convention (Aki & Richards, 2002; p. 101): $\lambda = 90° \pm 45°$ and $\lambda = -90° \pm 45°$ for reverse and normal mechanisms, respectively. Our subset of the SCARDEC catalog is restricted to earthquakes with depth shallower than 70 km.

The SCARDEC method retrieves STFs that can include early aftershocks, in particular for large earthquakes where the allowed STF duration is long (Vallée & Douet, 2016). As a consequence, such STFs do not represent a single rupture and thus do not follow the same relation between duration and seismic moment. We therefore excluded STFs where the moment rate goes to zero between distinct subevents. However, earthquakes with complex rupture time histories, including multiple peaks without significant intercancellation of the moment rate, are still present in the catalog. Our data set finally consists of 1,433 STFs whose magnitude distribution is reported in Figure 2a. The largest subduction earthquakes that occurred within the time period of our study are included in our catalog, except the 2004 Sumatra-Andaman M_w 9.1 earthquake, where the extremely long source duration prevented a reliable separation between the P and S teleseismic body waves. In the early part of the time period, fewer earthquakes are present because of the fewer available stations at that time. For this reason, the 1992 M_w 7.7 Nicaragua earthquake is, for example, not included in the SCARDEC database (Vallée & Douet, 2016).

The catalog includes earthquakes from different tectonic environments, but earthquakes occurring in subduction contexts are by far the most numerous ones. Most of these subduction earthquakes occur at the contact between the plates (as interface earthquakes), but stresses induced by the subduction process also generate intraplate events. Based on automated criteria, it is difficult to discriminate between interface and intraplate earthquakes (in particular intraslab earthquakes), because inaccuracies in the earthquakes location and mechanism can be misleading. For this reason, we performed a systematic examination of each earthquake, using SCARDEC and Global CMT (Ekström et al., 2012) solutions and, when available, some more detailed source descriptions. Using also the slab geometry from *slab1.0* (Hayes et al., 2012), it led us to a classification in four tectonic contexts: interface earthquakes, intraslab earthquakes, continental crust earthquakes, and oceanic crust earthquakes. Earthquakes occurring in the overriding plate of a subduction zone, in a continental rift, or more commonly in the context of continental convergence are included in the continental group. Normal earthquakes occurring in the outer rise of the subducting slab, in the context of oceanic ridges, and all other earthquakes occurring in the oceanic lithosphere are considered as oceanic events. This classification, together with SCARDEC's focal mechanism solutions, is represented on the map in Figure 3. The number of earthquakes in each group is reported in Table 1. It is noteworthy to mention that interface earthquakes represent 56% of the catalog, as reported in Table 1.

2.2. STF Impulsivity F_m^s

The STF integral is equal to the seismic moment, M_0, and its duration directly provides the earthquake duration. Under specific assumptions, the STF duration and peak can be related to the static stress drop $\Delta\sigma$ (e.g., Bilek et al., 2004; Houston, 2001, and with the SCARDEC database, Vallée, 2013). The stress drop is proportional to the strain drop $\Delta\epsilon = K\frac{D}{\tilde{L}}$, where K is a constant related to the fault geometry, D is the average slip, and $\tilde{L}$ is the smallest rupture dimension. It is expressed as follows:
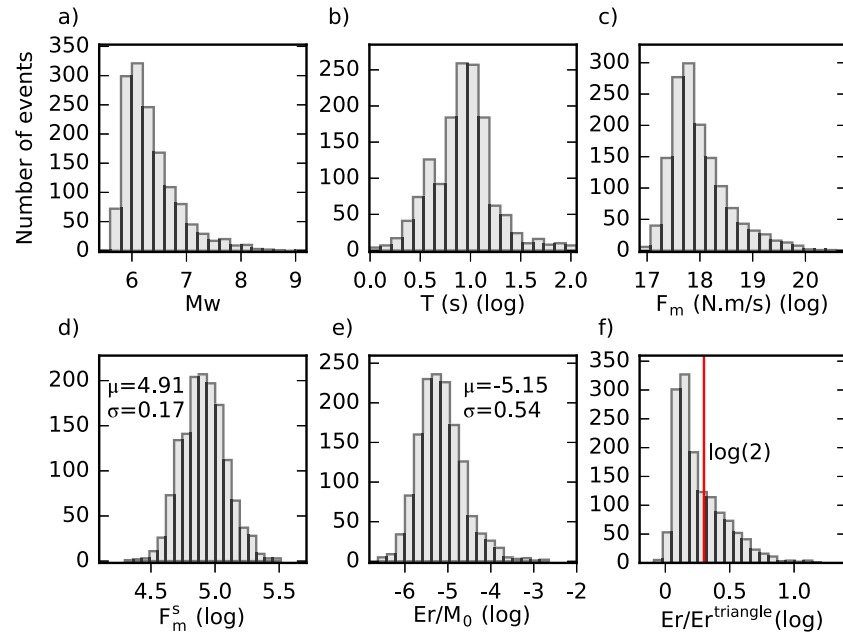
Figure 2. Distribution of earthquake source parameters for all our data set. (a) Moment magnitude M_w. (b, c) Logarithmic distributions of earthquakes source time function (STF) duration and STF peak. (d–f) Moment invariant source parameters analyzed in this study: impulsivity F_m^s, scaled energy $\frac{E_R}{M_0}$, and STF complexity index C_{ind}. In (d) and (e), μ and σ stand for logarithmic mean and standard deviation, respectively.

$$\Delta\sigma = \mu\Delta\epsilon = K\mu\frac{D}{\tilde{L}}. \tag{1}$$

In the case of a bidimensional rupture growth, $\tilde{L} = L$, where L is the characteristic fault length. The seismic moment can then be written as follows:

$$M_0 \propto \mu D L^2, \tag{2}$$

$$M_0 \propto \Delta\sigma L^3. \tag{3}$$

If we assume a constant rupture velocity V_r during the whole rupture process and neglect the rise time, the source duration T grows as $\frac{L}{V_r}$. Introducing this relation in equation 3, T can be written as a function of $\Delta\sigma$, V_r, and M_0 (e.g., Tanioka & Ruff, 1997):

$$T \propto \frac{M_0^{1/3}}{\Delta\sigma^{1/3}V_r}. \tag{4}$$

Table 1
Earthquakes Classification and Source Parameters

Subset	Number of earthquakes	$F_m^s : \mu\,(\sigma)$	$\frac{E_R}{M_0} : \mu\,(\sigma)$
All earthquakes	1,433	4.91 (0.17)	−5.15 (0.54)
Thrust mechanism	1,138	4.91 (0.17)	−5.18 (0.54)
Normal mechanism	295	4.94 (0.16)	−5.02 (0.49)
Interface	801	4.86 (0.15)	−5.34 (0.45)
Intraslab	186	5.03 (0.20)	−4.73 (0.70)
Continental crust	296	4.95 (0.15)	−5.01 (0.45)
Oceanic crust	150	4.97 (0.15)	−4.94 (0.44)

Note. Number of earthquakes, logarithmic average (μ), and standard deviation (σ) values for both F_m^s and $\frac{E_R}{M_0}$ are reported for the whole catalog and for each subset considered in this study.
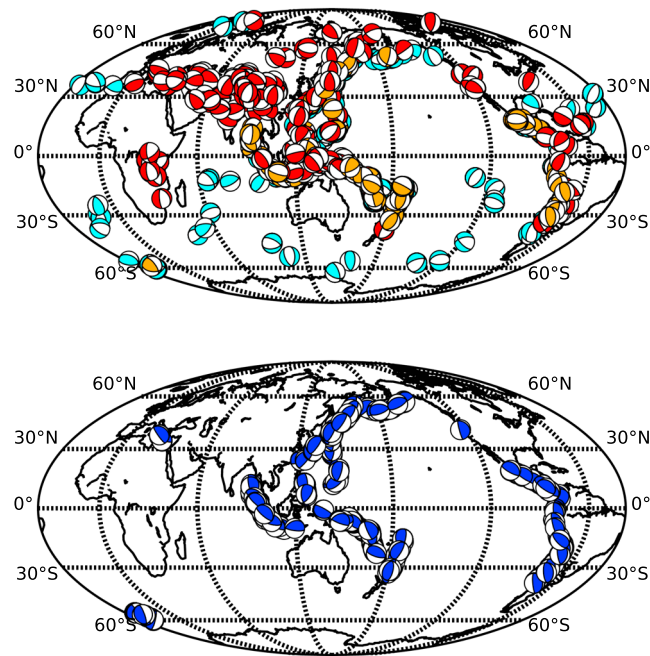
Figure 3. World map of the earthquakes (with their SCARDEC focal mechanisms) analyzed in this study. The color refers to the earthquake tectonic environment. (top) Continental crust (red), oceanic crust (light blue), and intraslab (yellow) earthquakes. (bottom) Interface earthquakes (blue).

The STF peak amplitude F_m ($= \max(\dot{M}(t))$, where $\dot{M}(t)$ is the moment rate function) is directly related to M_0 and T: $M_0 = CTF_m$, where C is a geometrical factor (e.g., $C = 0.5$ for a triangular STF). Assuming C is independent of the seismic moment, and using equation (4), the relation between M_0 and F_m can then be written as follows:

$$F_m \propto (\Delta \sigma V_r^3)^{\frac{1}{3}} Mo^{\frac{2}{3}}. \tag{5}$$

The classical hypotheses of constant rupture velocity and stress drop invariance with magnitude (self-similarity) lead to a constant product $\Delta \sigma V_r^3$. In this case, we have $T \propto Mo^{\frac{1}{3}}$ and $F_m \propto Mo^{\frac{2}{3}}$. We tested this hypothesis with F_m simply measured as the STF maximum and T as the time difference between the first and last point with amplitude higher than $0.1F_m$ and slope higher than 10% and 20% of the STF's maximum and minimum slopes, respectively.

On the whole data set, we find exponents close to the self-similarity assumption: $T \simeq Mo^{0.31}$ and $F_m \simeq Mo^{0.70}$. Both indicate a small increase of the product $\Delta \sigma V_r^3$ with magnitude, which might be explained either by V_r or $\Delta \sigma$. This can also be explained by the high-frequency depletion of STFs (see section 2.1.1), as it flattens and elongates the short duration STFs (corresponding to low-magnitude earthquakes). The observed relations are therefore used as scaling relationships, which is a way to compensate for the high-frequency depletion affecting small earthquakes.

Although derived in the same formalism, T and F_m are not sensitive to the same features of the rupture process. T reflects the full time history of the rupture, while F_m comes from the rupture areas generating the highest moment rate, due to their large slips and/or quick rupture velocities. They therefore provide similar information for a rupture breaking a simple patch, but in the presence of a long tail of low moment release (either real or due to unexplained data complexity), the T measurement leads to a long duration which is not representative of the main earthquake characteristics. The STF maximum F_m can be more objectively measured and is better related to the dominant features of the earthquake; additionally, even if its measurement is also subject to errors (e.g., attenuation and artificial complexities), their effects are less dramatic on the relation to seismic moment (Courboulex et al., 2016; Vallée, 2013). The higher variability observed for T than for F_m can be understood from these uncertainties related to the T measurement. This is also indicated by the lower quality of the linear regression for T ($C = 0.63$, with C being the determination coefficient) than for F_m ($C = 0.92$), as shown in Figure 4.
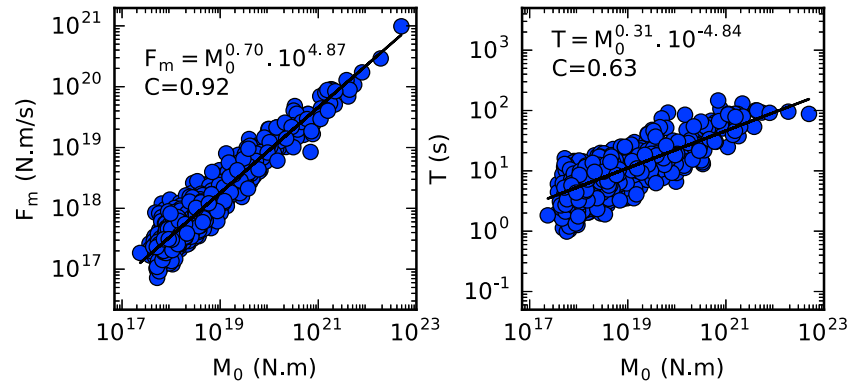
Figure 4. Moment dependence of the source time functions duration and peak. F_m (left) and T (right) are shown as a function of M_0 for the whole data set. Linear regressions performed on the parameters logarithms provide exponents close the values expected under a constant stress drop and rupture velocity hypothesis, with a better determination coefficient for F_m than for T.

The moment scaled peak, F_m^s, hereafter referred to as the earthquake impulsivity, is defined as

$$F_m^s = \frac{F_m}{M_0^{0.70}}, \tag{6}$$

$$F_m^s \propto \Delta\sigma^{\frac{1}{3}} V_r. \tag{7}$$

Any relative variation of the impulsivity hence results from a combined effect of stress drop and rupture velocity variations. A high F_m^s can result from a fast rupture velocity, a large slip with respect to the fault dimension (i.e., large strain drop), a high medium rigidity, or a combined effect of the three properties. In order to extract the single effect of $\Delta\sigma$ from F_m^s, an independent constraint on V_r is needed. Such information is actually provided by the ASTFs, and under several conditions (rupture propagation geometry and azimuthal coverage in particular), a quantitative estimate of V_r can be done. This analysis, beyond the scope of our study, can be found in Chounet et al. (2018), although on a reduced number of earthquakes. The variations of F_m^s are shown in Figure 2d for the whole data set. Due to its lognormal distribution, averages in log scale are hereafter considered.

2.3. Radiated Energy and the Complexity of STFs

The radiated energy, E_R, which is the part of the whole available energy released through seismic waves, can be measured from the moment rate functions (Bilek et al., 2004; Vassiliou & Kanamori, 1982)

$$E_R = \left[\frac{1}{15\pi\rho C_P^5} + \frac{1}{10\pi\rho C_S^5} \right] \int_0^T \ddot{M}(t)^2 dt, \tag{8}$$

where ρ, C_P, and C_S are the rock density, P, and S wave velocities, respectively. In their E_R measurements for shallow ($z \leq 60$ km) thrust earthquakes STFs in subduction zones, Bilek et al. (2004) used constant values of ρ, C_P, and C_S, because these properties are poorly constrained in the shallow Earth structure. For the same reasons, and to allow for comparisons, the same values are being considered in our calculations: $\rho = 2.8$ g/cm^3, $C_P = 6.9$ km/s, and $C_S = \frac{C_P}{\sqrt{3}}$. The E_R values are then used to compute the moment-scaled energy $\frac{E_R}{M_0}$. When multiplied by the rigidity μ, we obtain the apparent stress $\sigma_a = \mu \frac{E_R}{M_0}$, which is expected to be moment invariant under the self-similarity hypothesis (Kanamori & Anderson, 1975). Hence, $\frac{E_R}{M_0}$ and σ_a have long been analyzed to characterize seismic ruptures and compared with the earthquakes magnitude, faulting type, or depth (e.g., Choy & Boatwright, 1995; Choy & Kirby, 2004; Convers & Newman, 2011; Pérez-Campos & Beroza, 2001). In Figure 5, the scaled energy is shown against seismic moment for the whole data set and exhibits a slightly increasing trend with M_0, although with a large scatter. Such increase has actually been observed by several studies (e.g., Abercrombie, 1995; Kanamori et al., 1993; Mayeda et al., 2005). Ide and Beroza (2001) have pointed out that an increasing trend of the apparent stress with magnitude is expected when high-frequency attenuation affects the waveforms (see also section 2.2), as the latter effect has a larger role for short duration
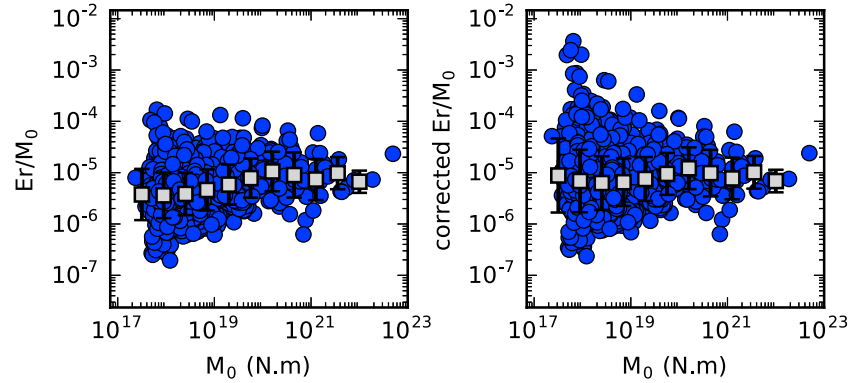
Figure 5. Moment dependence of the scaled radiated energy. $\frac{E_R}{M_0}$ versus M_0 is shown for the whole data set before (left) and after (right) correction for the high-frequency depletion above 0.5 Hz. Logarithmic average is represented with the gray squares.

earthquakes. After correction for the missing energy through a classical ω^{-2} model (Brune, 1970), they showed an invariance of $\frac{E_R}{M_0}$ over 17 orders of seismic moment. As seen in section 2.1.1, such high-frequency depletion is expected with average STFs. We here propose to correct for the missing energy following the methodology described by Ide and Beroza (2001). We assume that STFs spectra follow an ω^{-2} falloff which is interrupted above a given cutoff frequency f_{cut}. The fraction F of missing energy over total energy in this case depends both on the spectrum corner frequency f_c and the cutoff frequency f_{cut}: $F = 1 - \frac{2}{\pi}(\frac{(-x)}{(1+(x)^2)} + arctan(x))$, with $x = \frac{f_{cut}}{f_c}$. Practically, f_c is approximated by $\frac{1}{T}$, and f_{cut} is set to 0.5 Hz for all earthquakes. After this correction, the average trend of $\frac{E_R}{M_0}$ is flattened (Figure 5, right panel). A side effect of this correction is an increased variability of $\frac{E_R}{M_0}$ for small magnitudes. Indeed, among small earthquakes, the most radiative ones are the shortest ones, and as their associated STFs receive the highest correction, they have even higher radiated energies. For the whole catalog, the corrected $\frac{E_R}{M_0}$ average value is $7.1\ 10^{-6}$, consistent with previous studies (Bilek et al., 2004; Convers & Newman, 2011; Pérez-Campos & Beroza, 2001, for instance), and the distribution shown in Figure 2e exhibits a lognormally distributed parameter. In the following, we consider the corrected values of E_R.

Figure 6 shows $\frac{E_R}{M_0}$ against F_m^s: the parameters are strongly correlated and $\frac{E_R}{M_0}$ appears to grow as $F_m^{s\,3}$. This naturally comes from the equations, for instance, in the simple case of an isosceles triangular STF of peak F_m and area M_0. The radiated energy in this case is given by

$$E_R^{tri} = 2\left[\frac{1}{15\pi\rho C_P^5} + \frac{1}{10\pi\rho C_S^5}\right]\frac{F_m^3}{M_0}, \tag{9}$$

$$\frac{E_R^{tri}}{M_0} \simeq 2\left[\frac{1}{15\pi\rho C_P^5} + \frac{1}{10\pi\rho C_S^5}\right]F_m^{s\,3}. \tag{10}$$

The observed variability in Figure 6 is related to the complexity of the STFs, which can significantly differ from self-similar triangular shapes. This is first illustrated in Figure 1, where the three M_w 7 earthquakes have different STFs. The first STF (a) is the most impulsive and, as expected from equation (10), has the largest scaled energy ($\frac{E_R}{M_0} = 1.6\ 10^{-4}$); the other two, (b) and (c), share the same low impulsivity. However, the third one (c) has a more complex shape and is therefore associated with a larger radiated energy ($\frac{E_R}{M_0} = 2.7\ 10^{-5}$ compared to $\frac{E_R}{M_0} = 7.6\ 10^{-6}$). A similar example of this behavior is provided in Figure 6: at a given F_m^s, a function with several subevents and an overall rough shape is 3 times more radiative than a function with a single event. These observations support what can be inferred from equations (8) and (9): earthquakes with impulsive STFs, related to high slip rate and/or high rupture velocity, have the largest radiated energy, and among earthquakes with similar impulsivity, earthquakes exhibiting complex STFs (due to slip rate and/or rupture velocity variations) radiate more energy. The latter observation also offers a way to quantify the earthquake complexity through the computation of their radiated energy. As proposed by Bilek et al. (2004), this complexity can be quantified by the ratio between the radiated energy and a radiated energy reference, derived from
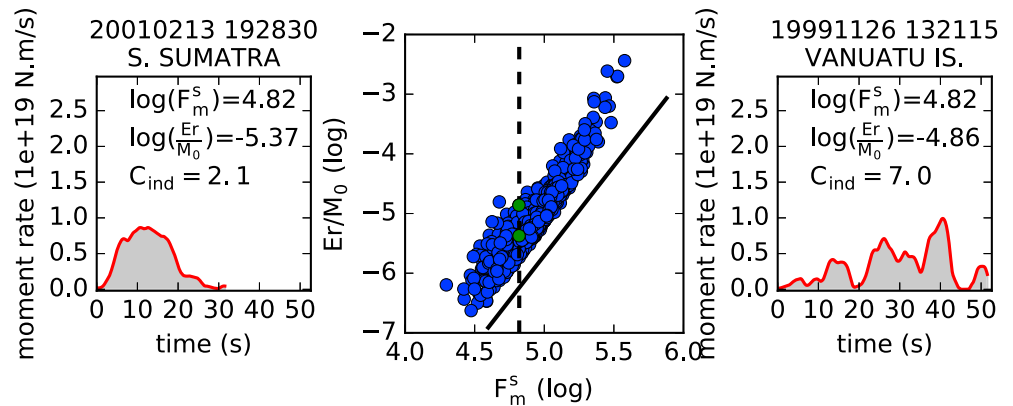
Figure 6. Relations between scaled radiated energy and impulsivity. (middle) $\frac{E_R}{M_0}$ versus F_m^s, showing that $\frac{E_R}{M_0}$ evolves as the cube of F_m^s. (left and right) Subplots that show two different source time functions sharing similar seismic moment and impulsivity but different scaled energy (represented by the green dots in the middle subplot). The right source time function exhibits higher radiations, which result from its complex rupture history.

an STF represented by an isosceles triangle with the same M_0 and F_m. A complexity index C_{ind} is then introduced by scaling E_R to the corresponding E_R^{tri} (computed from equation (9) and corrected from high-frequency depletion as E_R):

$$C_{ind} = \frac{E_R}{E_R^{tri}}. \tag{11}$$

The distribution of C_{ind} (Figure 2) shows that around one third of the catalog is associated with a complexity index above 2 (i.e., twice as more *complex* than an isosceles triangle). The STFs belonging to this subset have either two or more well-separated subevents (Figure 1c) and/or a rough character (Figure 6).

3. Global Observations

3.1. Depth and Focal Mechanism Dependencies

The source parameters F_m^s, $\frac{E_R}{M_0}$, and C_{ind} for the whole data set are shown as a function of depth in Figure 7. For both F_m^s and $\frac{E_R}{M_0}$, the dominant feature is their increase at depths larger than $z \simeq 40$ km, both for normal and reverse mechanisms (Figures 7a and 7b). This can be explained by the effect of the medium rigidity, which directly impacts $\Delta\sigma$ and influences the rupture velocities V_r. At crustal depths and along the subduction interface, the rigidity is expected to be largely context dependent, which may explain that this property does not have a clear signature on the average source parameters above $z \simeq 40$ km. On the contrary, below $z \simeq 40$ km, where only intraslab and interface earthquakes occur, the rigidity in the slabs and in the upper mantle is significantly larger and leads to the F_m^s and $\frac{E_R}{M_0}$ increase.

The depth evolution for thrust and normal mechanisms shows that the focal mechanism type does not have a large imprint on the source parameters. However, at shallow depths ($z \simeq 10$–20 km), where normal earthquakes are the most abundant, their impulsivity and scaled energy are larger than the one of thrust earthquakes. This small difference (also visible in the global Table 1) has been found in several other studies. For instance, the product $\Delta\sigma V_r^3$ from either moment scaled duration estimates (Houston, 2001) or corner frequency estimates (Allmann & Shearer, 2009) is found slightly lower for reverse faulting earthquakes than for normal faulting earthquakes. Analyses of the scaled energy (e.g., Convers & Newman, 2011; Pérez-Campos & Beroza, 2001) report a similar difference. Rather than an intrinsic difference between normal and thrust earthquakes, we underline in the next sections that this can be understood by the fact that subduction interface earthquakes (which are by definition thrust earthquakes) are less impulsive than all the other types of earthquakes. Complexity index reveals that, independently of the focal mechanisms, earthquakes become simpler with increasing depths (Figure 7c). We obtain a similar pattern as the one found by Bilek et al. (2004), based only on shallow thrust earthquakes in subduction zones.

3.2. Low Impulsivity of Subduction Interface Earthquakes

In Figures 7d–7f, the same source parameters are represented with respect to the four tectonic environments defined in section 2.1. Over the whole range of depths, the interface group includes on average ruptures
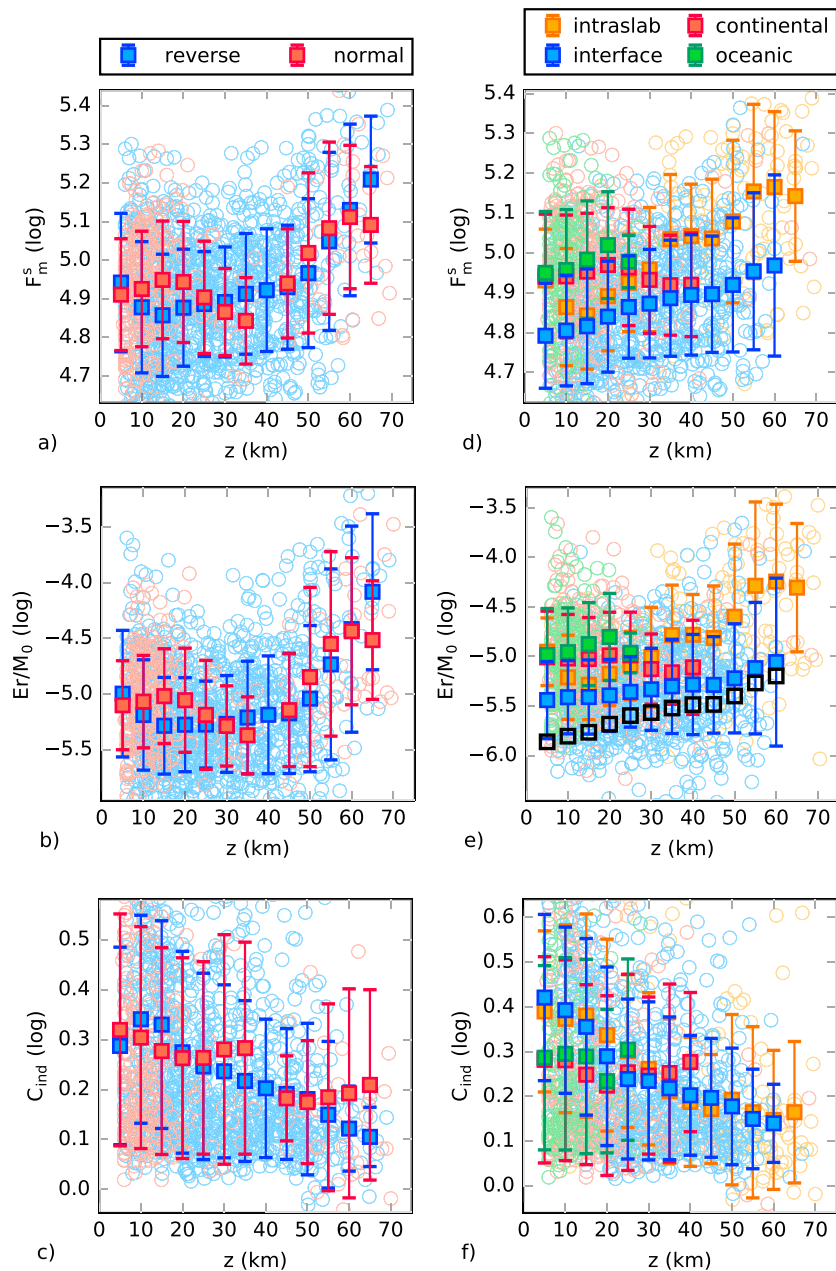
Figure 7. Depth dependence of the source parameters and influence of the earthquake type. F_m^s (a, d), $\frac{E_R}{M_0}$ (b, e), and C_{ind} (c, f) are shown as a function of depth for the whole data set, with the following additional separations: in (a)–(c), earthquakes are separated between normal and thrust faulting mechanisms; in (d)–(f), earthquakes are shown as a function of their tectonic environment. Interface earthquakes are characterized by a lower F_m^s and $\frac{E_R}{M_0}$, compared to the intraslab, continental crust, and oceanic crust earthquakes. Logarithmic averages over depth intervals and their corresponding standard deviations are computed for each considered category and represented by the squares. The black squares show the average values of $\frac{E_R^{tri}}{M_0}$ for the interface group, which are the values expected from F_m^s, and without complexity of the STF: without complexity and as a function of F_m^s, scaled radiated energy should increase from surface. Note that we focus here on the average trends, and extreme values of source parameters may fall out of the plot limits; extreme values are analyzed later on in the text.

with lower values of both impulsivity and scaled energy compared to the three other contexts. This behavior is especially striking at depth, when compared to intraslab earthquakes. On the contrary, earthquakes belonging to the oceanic group are the most impulsive and energetic in their depths range, that is, between surface and 25-km depth. Different features are observed for the complexity index. Its decrease with depth is observed similarly for interface and intraslab earthquakes, while its values are lower and more stable with depth for oceanic and continental earthquakes. From these observations, it appears that the tectonic environment has a stronger impact than the type of focal mechanism. This also explains why the simple classification in normal and reverse groups (Figures 7a and 7b), which hides the diversity of the tectonic environments, shows an irregular depth trend between 5 and 40 km. Taken independently, the interface group shows a continuous increase of F_m^s with depth, while $\frac{E_R}{M_0}$ values are more stable before increasing below $\simeq$ 45 km. This difference is underlined by the different depth trends observed between $\frac{E_R}{M_0}$ and $\frac{E_R^{tri}}{M_0}$ (Figure 7e), $\frac{E_R^{tri}}{M_0}$ varying as $F_m^{s\,3}$.

Consistent observations have been previously reported, based on other data set analyses. F_m^s increase with depth is consistent with the decrease of moment scaled durations with depth in subduction zones observed by Bilek and Lay (1999). Their observation of a sharp decrease between 5 and 20 km is interpreted as the effect of low rigidity materials in the shallow part of seismogenic zone. Compared to their observation, F_m^s variation in this depth range seems, however, weaker. This likely results from the intrinsic difference between peak and duration: at shallow depth, interface earthquakes are in general complex, which results in long durations, but does not necessarily affect the peak. This shallow complexity of interface earthquakes is also expected to increase $\frac{E_R}{M_0}$ values in spite of the weak F_m^s values. As pointed out by Bilek et al. (2004), this complexity compensates the long moment scaled durations (and similarly the low impulsivity) and explains why $\frac{E_R}{M_0}$ values do not clearly increase between surface and 45 km, while F_m^s and $\frac{E_R^{tri}}{M_0}$ do.

In one of the first global analyses of radiated energy, Choy and Boatwright (1995) observe that thrust earthquakes in subduction zones were associated with the lowest values of apparent stress. Based on STFs properties, Houston (2001) reported lower moment scaled durations for interplate thrust earthquakes than for intraplate thrust events. Allmann and Shearer (2009) also found lower stress drop values (from corner frequency estimates) for events in subduction zones compared to the other contexts. If we follow the assumption of a constant strain drop, as proposed by Vallée (2013), the small F_m^s and $\frac{E_R}{M_0}$ of interface earthquakes could be only due to the expected low rigidity in the hydrated region surrounding the interface. Other specific subduction properties could also explain the low values of both F_m^s and $\frac{E_R}{M_0}$. Fluid interaction with faults may weaken the frictional contact, as suggested by Houston (2001), which reduces the total available energy when the earthquake occurs. This observation can also originate from the maturity of subduction zones. Subduction plate boundaries are large and well-developed fault zones, having hosted a large number of earthquakes; as a consequence they can be considered as mature faults, contrary to young and/or slow fault systems where earthquakes are comparatively rare. This fault maturity leading to a smoothed surface, and hence a weaker fault zone in terms of strength, can lead to lower stress drop and apparent stress (e.g., Choy & Kirby, 2004; Houston, 2001).

4. Differences Among the Subduction Zones and Relations With Subduction Zone Properties

4.1. Interregion Variability of Subduction Interface Earthquakes

Subduction interface earthquakes are in average characterized by lower impulsivity and scaled radiated energy than other earthquakes. This results in a slightly lower variability of their impulsivity and scaled energy distributions (see Table 1 and Courboulex et al., 2016), which remains, however, strong. For example, interface earthquakes impulsivity varies from $10^{4.3}$ to $10^{5.47}$, which, converted into stress drop variations (basically, the cube of F_m^s), corresponds to 3 orders of magnitude difference. This variability could either be the result of an intrinsic variability observed at each subduction zone or it could either results from absolute differences between subduction zones. We propose here to characterize this variability by analyzing the variations of interface earthquakes source parameters among the different subduction zones. Interface earthquakes from our data set are mostly located in the Circum-Pacific and Indian Ocean megathrusts. Additionally, seven earthquakes are located in the Hellenic subduction zone (Mediterranean Basin) and eight earthquakes in the Sandwich subduction zone (South Atlantic). Earthquakes are divided into 18 segments of subduction zones,
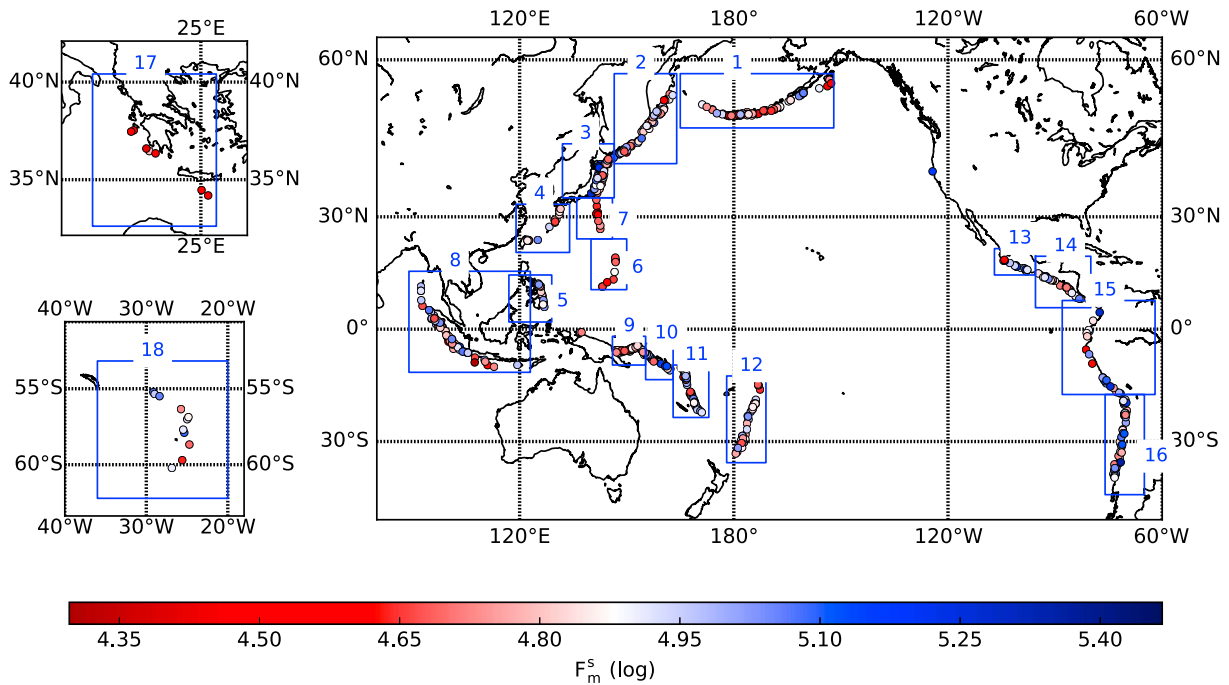
Figure 8. World map of interface earthquakes impulsivity F_m^s. The 18 subduction segments considered here are delimited by the blue boxes. 1: Aleutians Islands, 2: Kuril Islands, 3: Japan, 4: Ryukyu Islands, 5: Philippines, 6: Mariana Islands, 7: Izu-Bonin Islands, 8: Indonesia, 9: New Britain, 10: Solomon Islands, 11: Vanuatu, 12: Tonga-Kermadec, 13: Mexico, 14: Central America, 15: Colombia-Peru, 16: Chile, 17: Greece, 18: Sandwich Islands.

which are drawn on the map in Figure 8, showing the impulsivity of interface earthquakes. Depth plots of impulsivity and scaled radiated energy are provided for each segment in Figures 9 and 10. These figures first indicate differences between subduction segments in the behavior of both F_m^s and $\frac{E_R}{M_0}$ as a function of earthquakes depth. For example, Chile and Japan segments exhibit a clear increase of F_m^s and $\frac{E_R}{M_0}$ with depth, which is not observed for the Vanuatu and the New Britain Trench segments. Absolute level of F_m^s and $\frac{E_R}{M_0}$ appears also to differ between segments: for example, most earthquakes from the New Britain Trench segments lie below the depth-varying average of both F_m^s and $\frac{E_R}{M_0}$, while the opposite is found for the Chile segment (Figures 9 and 10). While some homogeneous features can be extracted from a subduction segment, we also report sharp along-strike variations. These variations can be seen in Figure 11, where earthquake impulsivity is shown versus along-strike projection of earthquake location.

In the following, these differences are further described in details and discussed in light of diverse subduction zones properties. Both the age of the subducting seafloor and the convergence rate vary strongly among subduction zones. These properties, which respectively control the loading rate and the slab buoyancy, may impact the rupture properties. Another important property of fault zones is the seismic coupling, which quantifies which part of the convergence is expected to be released seismically rather than aseismically. The coupling in subduction zones is variable among subductions and also within a given subduction segment, along-strike, and along-dip of the plate boundary. Possible relationships between these subduction properties and interface earthquakes properties are here investigated. In order to search for a relation between our observations and subduction zones properties, convergence rate, age of the subducting seafloor, and when available, the level of coupling of the interface are provided for each region of interest. Oceanic seafloor ages come from Müller et al. (2008), and convergence rates come from NNR-MORVEL reference model (Argus et al., 2011). We, accordingly, consider the plates system defined in the NNR-MORVEL reference model. In this section, we focus on the subduction zones with the lowest and highest values of F_m^s and $\frac{E_R}{M_0}$ and also on the segments exhibiting sharp along-strike and along-dip variations of these parameters. These observations are discussed in light of subduction zones properties in the next section.
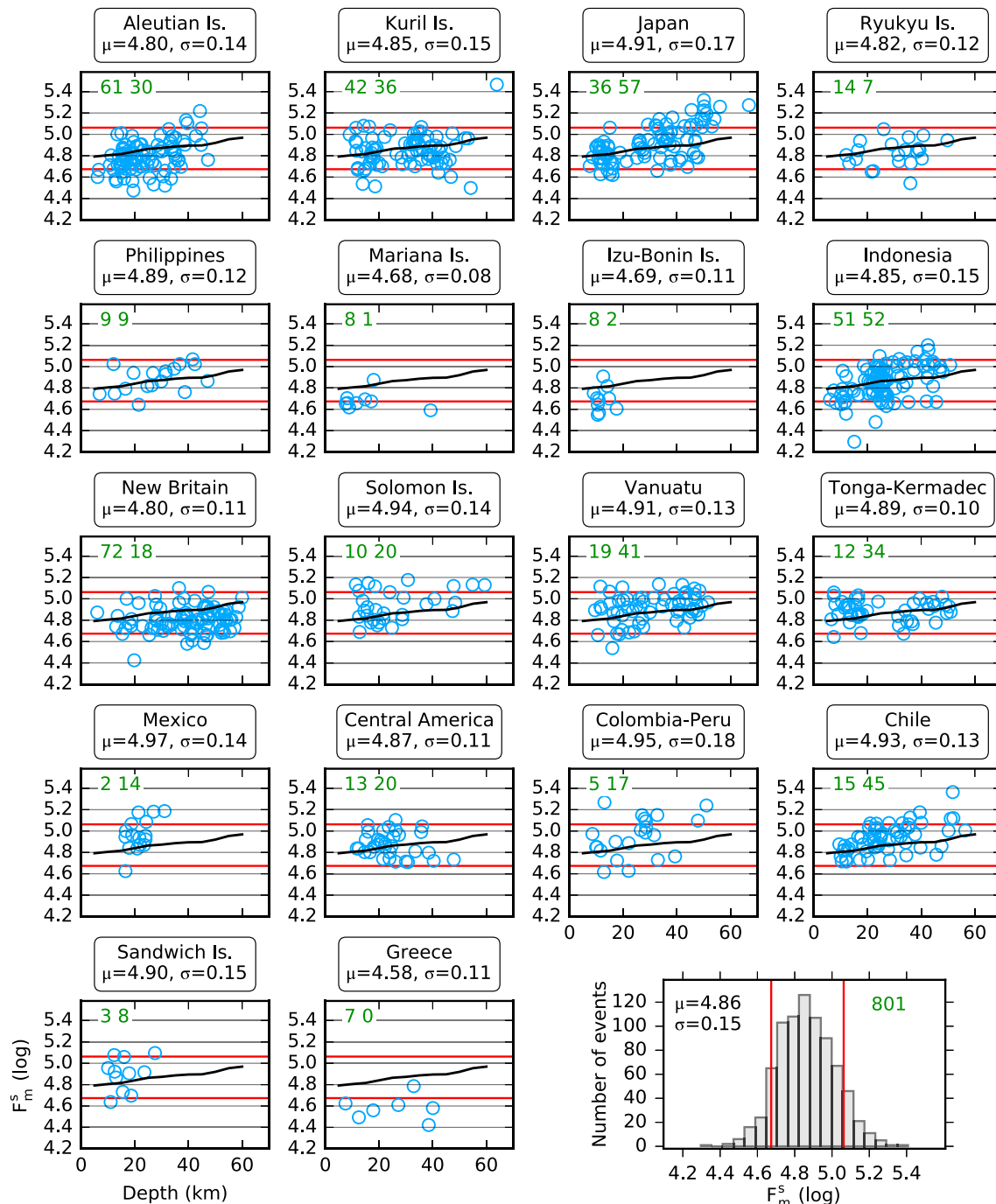
Figure 9. Impulsivity F_m^s versus earthquake depth for the interface earthquakes in each subduction segment (as defined in figure 8). The black curve in each subplot represents the depth-varying average (logarithmic) for the interface group. At the lower right corner of the figure, the F_m^s distribution of the 801 interface earthquakes is shown. The two vertical red lines stand for the first and last deciles of this distribution. F_m^s logarithmic average (μ) and standard deviation (σ) for each segment are reported in each subplot. The first and last deciles are reported on each subplot (red lines). In the upper left corner of each subplot, the number of earthquakes below and above the global average F_m^s (black curve) are indicated in green.
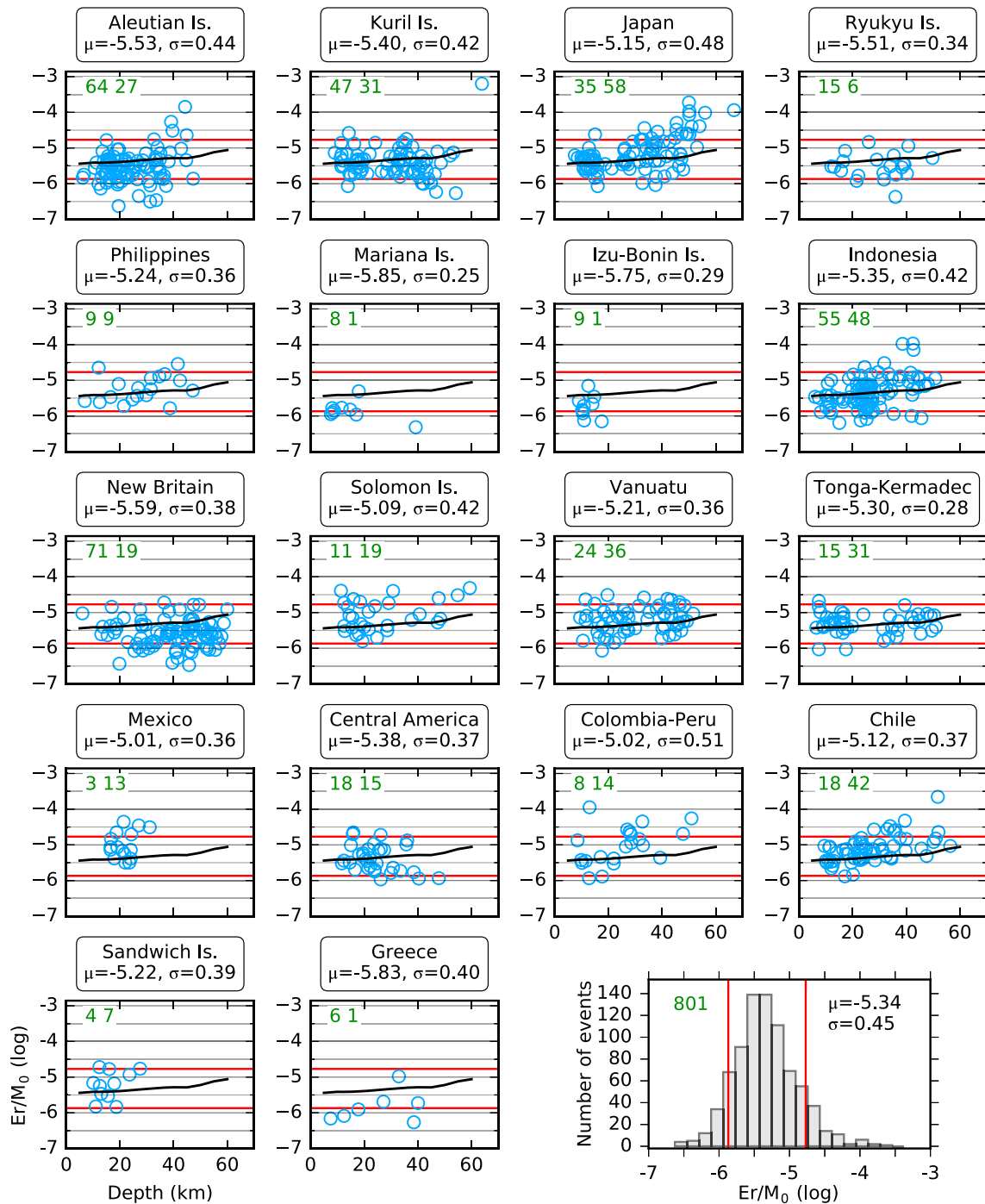
Figure 10. Same as Figure 9 but for the scaled radiated energy $\frac{E_R}{M_0}$.

4.1.1. Subduction Zones With Both Low F_m^s and $\frac{E_R}{M_0}$ Values

In four subduction segments, interface earthquakes impulsivity and scaled radiated energy are lower than those globally observed in subduction zones. These are the Izu-Bonin and Mariana subduction zones, the New Britain Trench, and the Hellenic subduction zone (see map in Figure 8).

4.1.1.1. Izu-Bonin and Mariana Arcs

These two contiguous segments have a northern limit located at the triple junction between the Pacific, Philippine Sea, and North American plates, and terminate to the South at the southern tip of the Mariana arc. In
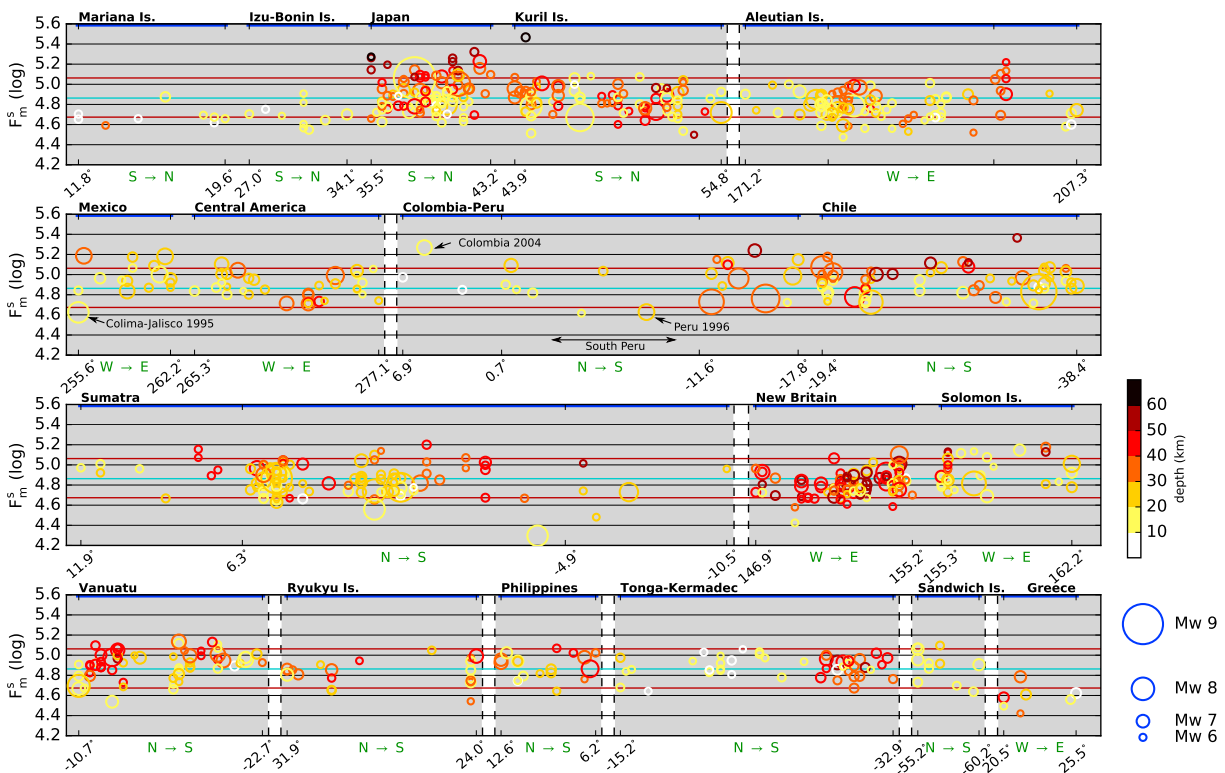
Figure 11. Along-strike variations of interface earthquakes impulsivity in the 18 subduction segments. Earthquake location is projected on the trench axis, and earthquake depth is indicated by the color scale. The moment magnitude is represented by the size of the circle. Along the *x* axis, latitude or longitude are provided as additional geographic information. Below each segment, the approximate orientation of the projection (e.g., "N→S") is reported in green. Zones separated by white vertical stripes are discontinuous (e.g., Sandwich Islands and Greece), while the other segments are spatially close to each other. Peculiar earthquakes and zones discussed in the text are indicated in the figure.

the Izu-Bonin and Mariana segments, the Pacific plate subducts below the Philippine plate with a low rate of convergence (4.8 ± 1.6 mm/year and 5.9 ± 7.6 mm/year, respectively), associated with a low level of seismic activity concentrated in a shallow depth range ($z \leq 30$ km in our catalog). The age of the subducting Pacific plate gradually decreases from 152 My to the south to 133 My to the north. No large historical earthquake is known, and this zone is thought to be almost uncoupled (Scholz & Campos, 1995). A large earthquake at its southern limit (the 1993 M_w 7.8 Guam earthquake) was first thought to be an interface earthquake (Campos et al., 1996), but more detailed analyses (Harada & Ishibashi, 2008) have favored an intraslab mechanism. In this region, despite the small number of earthquakes in our data set (19), we observe a clear dominance of earthquakes with low F_m^s and $\frac{E_R}{M_0}$. 17 earthquakes over 19 lie below depth-varying averages of F_m^s and $\frac{E_R}{M_0}$ (Figures 9 and 10). These two segments appear to produce poorly impulsive and also rather simple ruptures, as suggested by the very low values of $\frac{E_R}{M_0}$ (Figure 10). This observation agrees well with the long normalized source durations observed in this area by El Hariri et al. (2013) on subduction earthquakes.

4.1.1.2. New Britain Trench

In this segment, the Solomon Sea plate subducts below the South Bismarck Sea plate. Together with the Solomon Islands segment, this subduction zone is part of a very complex and active tectonic system. In the eastern part of the segment, the young Woodlark Basin (5 My) enters into the subduction below the Solomon Islands (Yoneshima et al., 2005). This bathymetric contrast is associated in our observations with a gradual increase of F_m^s from the New Britain Trench segment to the Solomon Islands segment (Figure 11). 72 earthquakes (over 90) correspond to ruptures with impulsivity and scaled energy below the depth-varying averages (Figures 9 and 10). Based on teleseismic source spectra analysis, Denolle and Shearer (2016) also report low values of stress drop and radiated energy in this subduction zone, with a similar increase when approaching the Solomon Islands. $\frac{E_R}{M_0}$ values are lower than expected by F_m^s values, which indicates that ruptures have simple time history ($C_{ind} \leq 2$ for 68 earthquakes over 90). Unlike other subduction segments, the seismogenic zone is deep (most depths are below 30 km) and plunges with a steep angle (earthquakes dip angle δ is

found close to $\delta \simeq 40°$). The strongly bent trench and the very young subducting seafloor (the oceanic crust is younger than $\simeq 28$ My; Honza et al., 1987) also contribute to the unique character of this subduction. The convergence rate of the Solomon Sea plate relative to the South Bismarck Sea plate is poorly known but must be faster than 70 mm/year (Tregoning & Gorbatov, 2004). Among the 18 segments analyzed here, this is the only one that hosts both a very dense and nonimpulsive seismicity.

4.1.1.3. Greece

The Hellenic plate boundary results from the subduction of the old Nubian plate (subducting Mediterranean Basin age is 254 ± 10 My) below the Aegean Sea at a rate of $\simeq 35$ mm/year (Reilinger et al., 2006). Our data set only includes seven earthquakes from this zone, but all lie below the average impulsivity values (Figure 9), and six of them have an impulsivity in the lowest 10% of the F_m^s distribution. In terms of scaled energy, $\frac{E_R}{M_0}$ values are low but higher than expected from F_m^s estimates (Figure 10), which corresponds to a high complexity level ($C_{ind} \geq 5$ for six of them). In the Hellenic subduction zone, the geodetic studies (Shaw & Jackson, 2010; Vernant et al., 2014) image a low coupled interface.

4.1.2. Subduction Zones With Both High F_m^s and $\frac{E_R}{M_0}$

On the other hand, we identify four subduction segments with values of F_m^s and $\frac{E_R}{M_0}$ higher than global averages of interface earthquakes. These are the Mexico, Chile, Solomon islands, and Vanuatu segments (see map in Figure 8).

4.1.2.1. Mexico

This segment involves the subduction of the Cocos plate beneath the North America plate, except at the northern edge where the small Riveras plate subducts beneath the North America plate. Its southern limit corresponds to the subduction of the Tehuantepec ridge, at 264°E. In this segment, the convergence rate is of 65 ± 4 mm/year, and the plunging oceanic crust is younger than 20 My (Couch & Woodcock, 1981). Plate interface is locked, according to Franco et al. (2005) and Correa-Mora et al. (2008) geodetic studies. Interface ruptures in this zone are for most of them (13 over 16) above the average impulsivity and scaled energy values (Figures 9 and 10). At the northwestern edge of the segment, the 1995 M_w 7.8 Colima-Jalisco earthquake is an exception with an impulsivity below the first decile (Figures 9 and 11). However, its scaled radiated energy is close to the average values (Figure 10), which results from its complex time history ($C_{ind} = 12.2$), distributed in three subevents (consistent with the study of Courboulex et al., 1997). Each subevent reaches a moment rate peak of $\simeq 1.5.10^{19}$ N.m/s. As a consequence, for each subevent, the actual impulsivity is $F_m^s \times 3 = 4.2.10^4 \times 3 \simeq 10^{5.1}$, which makes each individual subevent close to the average values. This earthquake illustrates the advantage of combining F_m^s and $\frac{E_R}{M_0}$ measurements which helps here to discriminate between poorly impulsive and complex ruptures.

4.1.2.2. Chile

The Chilean segment, where Nazca plate subducts below South America, hosts ruptures with high F_m^s (44 earthquakes over 60 above average) and $\frac{E_R}{M_0}$ (41 earthquakes over 60 above average), as reported in Figures 9 and 10. An increase with depth for both source parameters is observed below $\simeq 30$ km and appears sharper than the global trend (Figures 9 and 10). From geodetic data (Chlieh et al., 2011; Métois et al., 2016; Ruegg et al., 2009, for example), it is observed that the Chilean margin is almost fully coupled. In this segment of subduction, the plate convergence is 70 ± 6 mm/year, and the oceanic seafloor age is 43 ± 8 My. Due to the global behavior of the Chile, Mexico, and Colombia-Peru segments, the eastern Pacific subduction zones host more impulsive earthquakes than the western Pacific subduction zones. This feature is consistent with the observations of Denolle and Shearer (2016), who reported higher values of stress drop and radiated energy in the eastern Pacific relative to the western Pacific.

4.1.2.3. Solomon Islands

The Solomon Island segment is the southeastward continuation of the New Britain Trench. It results from the subduction of the Woodlark Basin microplate and the Australian plate beneath the Pacific plate, at a rapid rate of $\simeq 100$ mm/year. The Woodlark basin is a very young structure of $\simeq 5$ My (Yoneshima et al., 2005). This zone hosts a shallow seismicity, with impulsive ruptures, as almost one third of them are within the highest 10% of the F_m^s and $\frac{E_R}{M_0}$ distributions. This contrasts with the group of low impulsivity earthquakes uniformly found in the nearby New Britain Trench segment (Figure 11). This change in rupture properties is spatially associated with a subducting topographic structure, the ridge of the Woodlark basin.

4.1.2.4. Vanuatu

The Vanuatu segment is located along the southeastern continuation of the Solomon Islands segment and corresponds to the New Hebrides Trench. It involves the subduction of the Australian plate beneath the Pacific plate and the New Hebrides microplate. The convergence rate increases from 90 mm/year to the north to 128 mm/year to the south, and the age of the subducting oceanic crust is 34 ± 6 My. Interface earthquakes recorded in this zone have, for two thirds of them, values of F_m^s and $\frac{E_R}{M_0}$ above the average (Figures 9 and 10). However, at the northern edge of the segment, where the trench is curved, a cluster of lower impulsivity earthquakes is identified (Figure 11). Using geodetic measurements, Power et al. (2012) find a high coupling level between $-16°$S and $-18°$S latitude. Around this area, intermediate values of coupling are found at shallow depth.

4.1.3. Subduction Zones Including Strong Along-Strike or Along-Dip Variations

In 10 subduction segments, intermediate average values of F_m^s and $\frac{E_R}{M_0}$ are found, with large along-strike variations for some of them. We describe here the six segments where specific along-strike or along-dip variations occur.

4.1.3.1. Aleutian Islands

The Aleutian segment involves the subduction of the Pacific plate beneath the North America plate, at a convergence rate of 71 ± 4 mm/year, slightly increasing and becoming oblique in the western part. The age of the Pacific plate is about 50 to 60 My in this segment, increasing from east to west. The interface earthquakes in this segment exhibit in average low values of F_m^s and $\frac{E_R}{M_0}$ and also large along-strike variations. In the area between 170°E and 197°E, covering the 1965 M_w 8.7 and the 1957 M_w 8.6 ruptures, earthquake source parameters appear very scattered (Figure 11). In a subdomain of this area (between 186°E and 190°E), earthquakes are homogeneously characterized by a very low impulsivity. East of 197°E, in the Shumagin island area (between 198°E and 200°E), only deep ($z \simeq 40$ km) and impulsive earthquakes have been identified (Figure 11). At the eastern edge of Aleutian arc, off Kodiak island, low values of F_m^s and $\frac{E_R}{M_0}$ are observed at shallow depth ($z \leq 30$ km, Figure 11). Off Kodiak island, the interface is highly coupled (Zweck et al., 2001). The central part of the Aleutian arc is also coupled, owing to the large ruptures that occurred in this area.

4.1.3.2. Japan

The Japan subduction zone is here the small subduction segment where the Pacific plate subducts beneath Honshu and Hokkaido Islands. It hosts one tenth of all the interface earthquakes in our data set. The age of the Pacific plate is 131 ± 1 My, and the convergence rate is 92 ± 1 mm/year. The earthquake depth ranges from 5- to $\simeq$ 60-km depth. We observe in this subduction segment a positive trend of F_m^s and $\frac{E_R}{M_0}$ values with depth, starting from 30 km, which is stronger than the general depth increase. The clear increase of the product $\Delta\sigma V_r^3$ with depth has also been observed from regional (e.g., Uchide et al., 2014) and global studies (e.g., Denolle & Shearer, 2016). The 2011 M_w 9.1 Tohoku earthquake is here characterized by a large impulsivity (Figure 11), which is consistent with the compact and large slip observed from detailed source studies (e.g., Ide et al., 2011; Lay & Kanamori, 2011). Geodetic measurements from Hashimoto et al. (2009) and Suwa et al. (2006) indicate a locked interface over the whole region.

4.1.3.3. Indonesia

The Indonesia segment involves the subduction of the Indo-Autralian plate below the Eurasia plate. As mentioned earlier, the 2004 Sumatra-Andaman earthquake is not included in the SCARDEC catalog, because of its abnormally long duration. Along this subduction segment, the convergence rate decreases from $\simeq$ 73 mm/year to the east (Java Trench) to $\simeq$ 23 mm/year to the north (Andaman islands), where convergence becomes highly oblique. The age of the subducting Indo-Australian plate varies along the boundary, with intermediate values ($\simeq$ 50 My) in front of the Sumatra island and older values both north of Sumatra ($\simeq$ 75 My) and in the Java Trench, where it reaches $\simeq$ 140 My. The earthquakes in this wide zone fall in the average values but with a large variability. Within the 2004 Sumatra-Andaman rupture area, where few earthquakes are observed, all but one exhibit a rather impulsive STF (Figure 11). Within the area of 2005 M_w 8.6 Nias-Simeulue earthquake rupture (3°N to 1°S latitude), the dense seismicity is scattered, with adjacent low and high impulsivity earthquakes (Figure 11). Further south, the shallow 2010 M_w 7.8 Mentawai earthquake occurred near the trench and caused a large tsunami (Hill et al., 2012). Consistently, this earthquake is part of the lowest F_m^s earthquakes of our data set (Figure 11). Besides this tsunami earthquake, this area hosts a dense seismicity with variable values of source parameters. From geodetic observations, the area is found to be strongly coupled (Philibosian et al., 2014). South of Mentawai, in the area of Enggano island, seismicity is sparser but also more impulsive. The last subarea of the Indonesia subduction segment is the Java trench, where interplate

is thought to be poorly coupled (Scholz & Campos, 2012) and has hosted two tsunami earthquakes in the past decades, in 1994 and 2006. From our data set, the 2006 M_w 7.8 Java tsunami earthquake (Ammon et al., 2006) has an impulsivity far below all other interface earthquakes, explained by its very long duration (150 s) and a rather high complexity index (10.6) related to a strong STF roughness. The 1994 M_w 7.6 Java tsunami earthquake (Abercrombie et al., 2001), on the contrary, does not exhibit a very low value of F_m^s. Nevertheless, its complexity index is low (1.4), indicating a smooth rupture and low radiation relative to its impulsivity. Two different features associated with a tsunamigenic behavior are provided here: a very low impulsivity and, alternatively, a very smooth STF, both features inducing low $\frac{E_R}{M_0}$ ruptures. In total, five earthquakes over seven are below the average of F_m^s and $\frac{E_R}{M_0}$ (Figures 9 and 11) in the Java trench.

4.1.3.4. Tonga-Kermadec

Within the Tonga-Kermadec subduction, two parts can be distinguished. The part south of the Louisville Seamount chain ($-26°$S latitude) hosts a seismicity concentrated between 30- and 50-km depth, with intermediate values of F_m^s. The part north of Louisville Seamount chain hosts a shallow seismicity ($z \leq 20$ km), slightly more impulsive than the southern seismicity (Figure 11). Although shallower, this seismicity appears more energetic, which is in opposition with the global depth trend. The convergence of the Pacific plate beneath the Australian plate in this zone increases strongly toward the north, ranging from 80 to 120 mm/year in the southern part and from 120 to 260 mm/year in the northern part, where the trench is bent. Subducting Pacific plate age is 98 ± 6 My. Power et al. (2012) observed that south of the Louisville Seamount chain, coupling strongly decreases from north to south.

4.1.3.5. Central America

The Central America segment corresponds to the subduction of the Cocos plate below the North America and Caribbean plates. It starts south of the Tehuantepec ridge and ends south of Costa Rica. The relative plate motion of Cocos plate beneath North America and Caribbean plates is 70 ± 7 mm/year, and subducting oceanic crust age is 20 ± 6 My. For most earthquakes in this segment, values of F_m^s and $\frac{E_R}{M_0}$ are strong, except in front of Nicaragua (Figure 11), where the shallow M_w 7.7 Nicaragua 1992 tsunami earthquake occurred (Ihmlé, 1996; not included in our catalog because of a too poor station coverage). In this area where only intermediate depth ($z \simeq 35$ km, Figure 11) earthquakes are found, low values of F_m^s and $\frac{E_R}{M_0}$ are observed. Consistently, in the area of the 1992 rupture, Bilek et al. (2016) report low stress drop, and Convers and Newman (2011) report low scaled radiated energy. The seismogenic zone off Nicaragua is, in contrast to the whole Central America segment, almost fully decoupled, as observed with GPS by Correa-Mora et al. (2009). This sharp lateral contrast explains the apparent decrease of F_m^s and $\frac{E_R}{M_0}$ with depth (Figures 9 and 10).

4.1.3.6. Colombia-Peru

The Colombia-Peru segment involves the subduction of the Nazca plate below Colombia, Ecuador, and Peru (South America plate). The convergence rate is 61 ± 7.9 mm/year and the seafloor age is 38.8 ± 11.9 My. It generally hosts earthquakes with both F_m^s and $\frac{E_R}{M_0}$ values above the average for interface earthquakes: this is the case for 16 and 14 over 22 earthquakes for F_m^s and $\frac{E_R}{M_0}$, respectively (Figures 9 and 10). At the northern edge of the Colombia-Peru segment, the 15 November 2004 M_w 7.3 earthquake is even one of the most impulsive earthquakes of the interface global data set (Figure 11). However, the central part of this segment (in North Peru, between 3° and 11°, Figure 11) contrasts with this general trend. Two earthquakes there have very low F_m^s: a M_w 5.9 earthquake (26 March 2009, $z = 14$ km) and the 1996 tsunamigenic Peru earthquake (M_w 7.5; Ihmlé et al., 1998). This central part is known to be a poorly coupled area, while the surrounding segments to the north and to the south are locked (Nocquet et al., 2014).

4.2. Discussion: Correlations With Age, Convergence Rate, and Seismic Coupling
4.2.1. Plate Age and Convergence Rate

The convergence rate of subduction zones controls the loading rate and hence impacts the seismicity over the plate interface. From our data set, the slowest subduction zones (Mariana, Izu-Bonin, and Greece) host interface earthquakes with low impulsivity and scaled radiated energy. Fast subduction zones also appear to host impulsive and radiative earthquakes (Chile, Solomon Islands, Vanuatu, for example). However, a few counter examples are observed. The New Britain Trench segment hosts earthquakes with low impulsivity and low scaled radiated energy but undergoes a fast convergence rate (at least 70 mm/year). Additionally, several zones with intermediate values of F_m^s and $\frac{E_R}{M_0}$ are characterized by the highest rates of convergence, such as Japan and especially north Tonga. Even though a positive correlation between the subduction convergence rate and earthquakes impulsivity is suggested, it does not hold for several subductions.

The age of the subducting oceanic crust varies between a few millions years and several hundreds of millions years. The old cold slabs are associated with higher rock density, decreasing the buoyant force of the slab over the interface and hence the normal stress over the interface. At first order, the eastern Pacific margin consists of younger slabs than the western margin and hosts more impulsive interface earthquakes (Mexico and Chile, and apart from local areas of low impulsivity earthquakes, Central America and Colombia-Peru). The Solomon Islands and the Vanuatu subductions are also subductions involving young oceanic plates and both impulsive and radiative earthquakes. Thus, young slabs appear to favor ruptures with strong impulsivity and radiated energy. Three subduction segments over four associated with both low F_m^s and $\frac{E_R}{M_0}$ earthquakes (Mariana, Izu-Bonin, and Greece) are also associated with the oldest subducting slabs. This suggests a negative correlation between plate age and source parameters F_m^s and $\frac{E_R}{M_0}$. However, the New Britain Trench again constitutes an exception as it is associated with a very young ($\leq$ 28 My) subducting seafloor and low F_m^s and $\frac{E_R}{M_0}$ earthquakes. We can also remark that old slabs are not systematically associated with low F_m^s and $\frac{E_R}{M_0}$ earthquakes. For example, the slab involved in the Japan subduction segment is among the oldest subducting slabs, and the segment hosts earthquakes with intermediate to high values of F_m^s and $\frac{E_R}{M_0}$ compared to the global average of interface earthquakes. The age of the subducting seafloor partially correlates with our observations of F_m^s and $\frac{E_R}{M_0}$; this large scale feature cannot, however, be responsible for local along-strike variations of rupture properties that are observed in several subduction segments.

4.2.2. Seismic Coupling

The seismic coupling of subduction zones is a large-scale property of plate interface but also varies regionally along-strike and along-dip of the interface. We here discuss a possible link between our observations and the available measurements of coupling that we reported from the literature in section 4.1. At a large scale, Mariana, Izu-Bonin, and the Greece subduction segments are found to be poorly coupled. Hence, three over four zones including the lowest average values of both F_m^s and $\frac{E_R}{M_0}$ are also poorly coupled. Consistently, the local coupled area at the southern edge of the Mariana subduction zone hosted a large earthquake with higher value of F_m^s and $\frac{E_R}{M_0}$ (see section 4.1.1.1). As no reliable coupling information was found for the New Britain Trench segment, this interesting case unfortunately cannot be discussed here. At the scale of intrasegment variations, low coupling also coincides with earthquakes of low level of impulsivity and scaled radiated energy. The clearest example is in front of Nicaragua, where we could identify ruptures of both low F_m^s and $\frac{E_R}{M_0}$ around $\simeq$ 30 km depth in an uncoupled area, where the 1992 Nicaragua tsunami earthquake occurred at shallower depth. In addition, in the poorly coupled Java and North Peru segments, the few interface earthquakes included in our data set have overall low values of F_m^s and $\frac{E_R}{M_0}$. This includes the 2006 Java tsunami earthquake, characterized by the lowest F_m^s of our data set (Figure 11), in agreement with its extremely long duration. Among the impulsive subduction zones, Mexico, Chile, and also the Central America and Colombia-Peru segments (except North Peru and Nicaragua areas) are found highly coupled.

These observations suggest a positive correlation between coupling and earthquake impulsivity and scaled radiated energy, both at large and local scales. Several ruptures with low F_m^s and $\frac{E_R}{M_0}$, however, do occur in coupled areas, such as the tsunamigenic 2010 M_w 7.8 Mentawai earthquake, in the Indonesia segment (see Figure 11). They, however, occurred in area of scattered distribution of the source parameters, which do not exhibit a homogeneous behavior. A more puzzling counter example of the apparent correlation between coupling and our earthquakes parameters is found in the Aleutian segment, near the Kodiak island. The coupling there is found locally high, but shallow and intermediate ($z \leq 40$ km) earthquakes are characterized by a low impulsivity. Other zones of high coupling can produce earthquakes with intermediate impulsivity (rather than high), such as the Japan subduction. However, compared to the eastern Pacific subductions, the subducting oceanic crust of this segment is much older, which, as proposed in section 4.2.1, may have a large-scale effect favoring low F_m^s and $\frac{E_R}{M_0}$ ruptures.

Overall, our observations in subduction zones indicate a positive correlation between coupling and earthquakes impulsivity as well as scaled radiated energy. Interestingly, based on the analysis of earthquakes moment tensors in global subduction zones, the recent study of Hardebeck and Loveless (2018) finds that poorly coupled subduction zones are also more poorly oriented for failure than highly coupled subduction zones. Interpreted in terms of relative strength, they propose that poorly coupled subduction zones are weaker in terms of strength than highly coupled subduction zones. If we admit that weaker faults favor low stress drops relative to stronger faults, this feature could explain the observed link between coupling and both earthquake impulsivity and scaled radiated energy.

5. Conclusion

In this study, we used STFs from the SCARDEC database in order to characterize the properties of dip-slip earthquakes and in particular the properties of subduction interface earthquakes. The measurement of the STF impulsivity, which is the moment scaled peak of the STF, provides a parameter that quantifies the relative variations of the product $\Delta\sigma V r^3$; when compared to scaled radiated energy, it also provides information on the complexity of the rupture. At the global scale and for shallow depth earthquakes (≤ 70 km), the major factor controlling the impulsivity and scaled radiated energy values is the tectonic environment rather than the earthquakes focal mechanism. Thrust interface earthquakes in subduction zones are more likely to rupture with both low impulsivity and scaled radiated energy than earthquakes in other tectonic settings. This likely results from the presence of hydrated sediments in the interface and/or from the maturity of subduction plate boundaries.

Among the 801 subduction interface earthquakes of our catalog, a large variability persists. We find that some regions exhibit in average low (Izu-Bonin, Mariana, Greece, and New Britain Trench) or high (Chile, Mexico, Vanuatu, and Solomon Islands) values of impulsivity and scaled radiated energy compared to the global average for interface earthquakes. The western Pacific subduction zones host earthquakes with lower F_m^s and $\frac{E_R}{M_0}$ than the eastern Pacific subduction zones, suggesting at a large scale a negative correlation between plate age and earthquakes impulsivity. At both global and local scales, our observations further indicate a positive correlation between earthquakes impulsivity and interface coupling. Impulsive segments are generally associated with high degree of coupling, while nonimpulsive ones are associated with low degree of coupling. We also find that local areas with low coupling (Nicaragua, North Peru, and Java Trench) correlate with a reduced earthquake impulsivity. The complex behavior of the Indonesia segment, which includes both impulsive and nonimpulsive earthquakes, and of some specific areas (in particular Kodiak Island along the Aleutian segment), however, indicate that coupling is not the unique factor controlling earthquake impulsivity.

References

Abercrombie, R. E. (1995). Earthquake source scaling relationships from -1 to 5 m_l using seismograms recorded at 2.5-km depth. *Journal of Geophysical Research*, *100*(B12), 24,015–24,036.

Abercrombie, R. E., Antolik, M., Felzer, K., & Ekström, G. (2001). The 1994 Java tsunami earthquake: Slip over a subducting seamount. *Journal of Geophysical Research*, *106*(B4), 6595–6607.

Abercrombie, R. E., & Rice, J. R. (2005). Can observations of earthquake scaling constrain slip weakening? *Geophysical Journal International*, *162*(2), 406–424.

Aki, K., & Richards, P. G. (2002). *Quantitative seismology*. California, United States: University Science Books.

Allmann, B. P., & Shearer, P. M. (2009). Global variations of stress drop for moderate to large earthquakes. *Journal of Geophysical Research*, *114*, B01310. https://doi.org/10.1029/2008JB005821

Ammon, C. J., Kanamori, H., Lay, T., & Velasco, A. A. (2006). The 17 July 2006 Java tsunami earthquake. *Geophysical Research Letters*, *33*, L24308. https://doi.org/10.1029/2006GL028005

Argus, D. F., Gordon, R. G., & DeMets, C. (2011). Geologically current motion of 56 plates relative to the no-net-rotation reference frame. *Geochemistry, Geophysics, Geosystems*, *12*, Q11001. https://doi.org/10.1029/2011GC003751

Bassin, C., Laske, G., & Masters, G. (2000). The current limits of resolution for surface wave tomography in North America. EOS Trans. AGU 81: Fall Meet, Suppl., Abstract.

Bilek, S. L., & Lay, T. (1999). Rigidity variations with depth along interplate megathrust faults in subduction zones. *Nature*, *400*(6743), 443–446.

Bilek, S., Lay, T., & Ruff, L. (2004). Radiated seismic energy and earthquake source duration variations from teleseismic source time functions for shallow subduction zone thrust earthquakes. *Journal of Geophysical Research*, *109*, B09308. https://doi.org/10.1029/2004JB003039

Bilek, S. L., Rotman, H. M., & Phillips, W. S. (2016). Low stress drop earthquakes in the rupture zone of the 1992 Nicaragua tsunami earthquake. *Geophysical Research Letters*, *43*, 10,180–10,188. https://doi.org/10.1002/2016GL070409

Brune, J. N. (1970). Tectonic stress and the spectra of seismic shear waves from earthquakes. *Journal of Geophysical Research*, *75*(26), 4997–5009.

Campos, J., Madariaga, R., & Scholz, C. (1996). Faulting process of the August 8, 1993, Guam earthquake: A thrust event in an otherwise weakly coupled subduction zone. *Journal of Geophysical Research*, *101*(B8), 17,581–17,596.

Chlieh, M., Perfettini, H., Tavera, H., Avouac, J.-P., Remy, D., Nocquet, J.-M., et al. (2011). Interseismic coupling and seismic potential along the central andes subduction zone. *Journal of Geophysical Research*, *116*, B12405. https://doi.org/10.1029/2010JB008166

Chounet, A., Vallée, M., Causse, M., & Courboulex, F. (2018). Global catalog of earthquake rupture velocities shows anticorrelation between stress drop and rupture velocity. *Tectonophysics*, *733*, 148–158.

Choy, G. L., & Boatwright, J. L. (1995). Global patterns of radiated seismic energy and apparent stress. *Journal of Geophysical Research (1978–2012)*, *100*(B9), 18,205–18,228.

Choy, G. L., & Kirby, S. H. (2004). Apparent stress, fault maturity and seismic hazard for normal-fault earthquakes at subduction zones. *Geophysical Journal International*, *159*(3), 991–1012.

Convers, J., & Newman, A. (2011). Global evaluation of large earthquake energy from 1997 through mid-2010. *Journal of Geophysical Research*, *116*, B08304. https://doi.org/10.1029/2010JB007928

Correa-Mora, F., DeMets, C., Alvarado, D., Turner, H., Mattioli, G., Hernandez, D., et al. (2009). Gps-derived coupling estimates for the Central America subduction zone and volcanic arc faults: El Salvador, Honduras and Nicaragua. *Geophysical Journal International*, *179*, 1279–1291.

Correa-Mora, F., DeMets, C., Cabral-Cano, E., Marquez-Azua, B., & Diaz-Molina, O. (2008). Interplate coupling and transient slip along the subduction interface beneath Oaxaca, Mexico. *Geophysical Journal International*, *175*(1), 269–290.

Couch, R., & Woodcock, S. (1981). Gravity and structure of the continental margins of southwestern Mexico and northwestern Guatemala. *Journal of Geophysical Research*, *86*(B3), 1829–1840.

Courboulex, F., Singh, S. K., Pacheco, J. F., & Ammon, C. J. (1997). The 1995 Colima-Jalisco, Mexico, earthquake (M_w 8): A study of the rupture process. *Geophysical Research Letters*, *24*(9), 1019–1022.

Courboulex, F., Vallée, M., Causse, M., & Chounet, A. (2016). Stress-drop variability of shallow earthquakes extracted from a global database of source time functions. *Seismological Research Letters*, *84*, 912–918.

Denolle, M. A., & Shearer, P. M. (2016). New perspectives on self-similarity for shallow thrust earthquakes. *Journal of Geophysical Research: Solid Earth*, *121*, 6533–6565. https://doi.org/10.1002/2016JB013105

Duputel, Z., Tsai, V. C., Rivera, L., & Kanamori, H. (2013). Using centroid time-delays to characterize source durations and identify earthquakes with unique characteristics. *Earth and Planetary Science Letters*, *374*, 92–100.

Ekström, G., Nettles, M., & Dziewoński, A. (2012). The global CMT project 2004–2010: Centroid-moment tensors for 13,017 earthquakes. *Physics of the Earth and Planetary Interiors*, *200*, 1–9.

El Hariri, M., Bilek, S. L., DeShon, H. R., Engdahl, E. R., & Bisrat, S. (2013). Along-strike variability of rupture duration in subduction zone earthquakes. *Journal of Geophysical Research: Solid Earth*, *118*, 646–664. https://doi.org/10.1029/2012JB009548

Franco, S., Kostoglodov, V., Larson, K., Manea, V., Manea, M., & Santiago, J. (2005). Propagation of the 2001–2002 silent earthquake and interplate coupling in the Oaxaca subduction zone, Mexico. *Earth, Planets and Space*, *57*(10), 973–985.

Harada, T., & Ishibashi, K. (2008). Interpretation of the 1993, 2001, and 2002 Guam earthquakes as intraslab events by a simultaneous relocation of the mainshocks, aftershocks, and background earthquakes. *Bulletin of the Seismological Society of America*, *98*(3), 1581–1587.

Hardebeck, J. L., & Loveless, J. P. (2018). Creeping subduction zones are weaker than locked subduction zones. *Nature Geoscience*, *11*(1), 60–64.

Hashimoto, C., Noda, A., Sagiya, T., & Matsu'ura, M. (2009). Interplate seismogenic zones along the Kuril-Japan trench inferred from GPS data inversion. *Nature Geoscience*, *2*(2), 141–144.

Hayes, G. P., Wald, D. J., & Johnson, R. L. (2012). Slab1. 0: A three-dimensional model of global subduction zone geometries. *Journal of Geophysical Research*, *117*, B01302. https://doi.org/10.1029/2011JB008524

Hill, E., Borrero, J. C., Huang, Z., Qiu, Q., Banerjee, P., Natawidjaja, D. H., et al. (2012). The 2010 M_w 7.8 Mentawai earthquake: Very shallow source of a rare tsunami earthquake determined from tsunami field survey and near-field GPS data. *Journal of Geophysical Research*, *117*, B06402. https://doi.org/10.1029/2012JB009159

Honza, E., Davies, H., Keene, J., & Tiffin, D. (1987). Plate boundaries and evolution of the Solomon Sea region. *Geo-Marine Letters*, *7*(3), 161–168.

Houston, H. (2001). Influence of depth, focal mechanism, and tectonic setting on the shape and duration of earthquake source time functions. *Journal of Geophysical Research*, *106*(B6), 11,137–11,150.

Ide, S. (2013). The proportionality between relative plate velocity and seismicity in subduction zones. *Nature Geoscience*, *6*(9), 780–784.

Ide, S., Baltay, A., & Beroza, G. C. (2011). Shallow dynamic overshoot and energetic deep rupture in the 2011 M_w 9.0 Tohoku-oki earthquake. *Science*, *332*(6036), 1426–1429.

Ide, S., & Beroza, G. C. (2001). Does apparent stress vary with earthquake size? *Geophysical Research Letters*, *28*(17), 3349–3352.

Ihmlé, P. F. (1996). Monte carlo slip inversion in the frequency domain: Application to the 1992 Nicaragua slow earthquake. *Geophysical Research Letters*, *23*(9), 913–916.

Ihmlé, P. F., Gomez, J.-M., Heinrich, P., & Guibourg, S. (1998). The 1996 Peru tsunamigenic earthquake: Broadband source process. *Geophysical Research Letters*, *25*(14), 2691–2694.

Kanamori, H., & Anderson, D. L. (1975). Theoretical basis of some empirical relations in seismology. *Bulletin of the Seismological Society of America*, *65*(5), 1073–1095.

Kanamori, H., Mori, J., Hauksson, E., Heaton, T. H., Hutton, L. K., & Jones, L. M. (1993). Determination of earthquake energy release and ML using TERRAscope. *Bulletin of the Seismological Society of America*, *83*(2), 330–346.

Kennett, B., & Engdahl, E. (1991). Traveltimes for global earthquake location and phase identification. *Geophysical Journal International*, *105*(2), 429–465.

Lay, T., & Kanamori, H. (2011). Insights from the great 2011 Japan earthquake. *Physics Today*, *64*(12), 33–39.

Lay, T., Kanamori, H., Ammon, C. J., Koper, K. D., Hutko, A. R., Ye, L., et al. (2012). Depth-varying rupture properties of subduction zone megathrust faults. *Journal of Geophysical Research*, *117*, B04311. https://doi.org/10.1029/2011JB009133

Madariaga, R. (1976). Dynamics of an expanding circular fault. *Bulletin of the Seismological Society of America*, *66*(3), 639–666.

Mai, P. M., & Thingbaijam, K. (2014). SRCMOD: An online database of finite-fault rupture models. *Seismological Research Letters*, *85*(6), 1348–1357.

Mayeda, K., Gök, R., Walter, W. R., & Hofstetter, A. (2005). Evidence for non-constant energy/moment scaling from coda-derived source spectra. *Geophysical Research Letters*, *32*, L10306. https://doi.org/10.1029/2005GL022405

Melgar, D., & Hayes, G. P. (2017). Systematic observations of the slip pulse properties of large earthquake ruptures. *Geophysical Research Letters*, *44*, 9691–9698. https://doi.org/10.1002/2017GL074916

Métois, M., Vigny, C., & Socquet, A. (2016). Interseismic coupling, megathrust earthquakes and seismic swarms along the chilean subduction zone (38–18 s). *Pure and Applied Geophysics*, *173*(5), 1431–1449.

Müller, G. (1985). The reflectivity method—A tutorial. *Journal of Geophysics-Zeitschrift Fur Geophysik*, *58*(1-3), 153–174.

Müller, R. D., Sdrolias, M., Gaina, C., Steinberger, B., & Heine, C. (2008). Long-term sea-level fluctuations driven by ocean basin dynamics. *science*, *319*(5868), 1357–1362.

Nishikawa, T., & Ide, S. (2014). Earthquake size distribution in subduction zones linked to slab buoyancy. *Nature Geoscience*, *7*(12), 904–908.

Nocquet, J.-M., Villegas-Lanza, J., Chlieh, M., Mothes, P., Rolandone, F., Jarrin, P., et al. (2014). Motion of continental slivers and creeping subduction in the northern Andes. *Nature Geoscience*, *7*(4), 287–291.

Pérez-Campos, X., & Beroza, G. C. (2001). An apparent mechanism dependence of radiated seismic energy. *Journal of Geophysical Research*, *106*(B6), 11,127–11,136.

Philibosian, B., Sieh, K., Avouac, J.-P., Natawidjaja, D. H., Chiang, H.-W., Wu, C.-C., et al. (2014). Rupture and variable coupling behavior of the Mentawai segment of the Sunda megathrust during the supercycle culmination of 1797 to 1833. *Journal of Geophysical Research: Solid Earth*, *119*, 7258–7287. https://doi.org/10.1002/2014JB011200

Power, W., Wallace, L., Wang, X., & Reyners, M. (2012). Tsunami hazard posed to New Zealand by the Kermadec and Southern New Hebrides subduction margins: An assessment based on plate boundary kinematics, interseismic coupling, and historical seismicity. *Pure and Applied Geophysics*, *169*(1-2), 1–36.

Prejean, S. G., & Ellsworth, W. L. (2001). Observations of earthquake source parameters at 2 km depth in the Long Valley Caldera, eastern California. *Bulletin of the Seismological Society of America*, *91*(2), 165–177.

Reilinger, R., McClusky, S., Vernant, P., Lawrence, S., Ergintav, S., Cakmak, R., et al. (2006). Gps constraints on continental deformation in the Africa-Arabia-Eurasia continental collision zone and implications for the dynamics of plate interactions. *Journal of Geophysical Research*, *111*, B05411. https://doi.org/10.1029/2005JB004051

Ruegg, J., Rudloff, A., Vigny, C., Madariaga, R., De Chabalier, J., Campos, J., et al. (2009). Interseismic strain accumulation measured by GPS in the seismic gap between Constitución and Concepción in Chile. *Physics of the Earth and Planetary Interiors*, *175*(1-2), 78–85.

Scholz, C., & Campos, J. (1995). On the mechanism of seismic decoupling and back arc spreading at subduction zones. *Journal of Geophysical Research*, *100*(B11), 22,103–22,115. https://doi.org/10.1029/95JB01869

Scholz, C. H., & Campos, J. (2012). The seismic coupling of subduction zones revisited. *Journal of Geophysical Research*, *117*, B05310. https://doi.org/10.1029/2011JB009003

Shaw, B., & Jackson, J. (2010). Earthquake mechanisms and active tectonics of the Hellenic subduction zone. *Geophysical Journal International*, *181*(2), 966–984.

Suwa, Y., Miura, S., Hasegawa, A., Sato, T., & Tachibana, K. (2006). Interplate coupling beneath NE Japan inferred from three-dimensional displacement field. *Journal of Geophysical Research*, *111*, B04402. https://doi.org/10.1029/2004JB003203

Tanioka, Y., & Ruff, L. J. (1997). Source time functions. *Seismological Research Letters*, *68*(3), 386–400.

Tregoning, P., & Gorbatov, A. (2004). Evidence for active subduction at the New Guinea trench. *Geophysical Research Letters*, *31*, L13608. https://doi.org/10.1029/2004GL020190

Uchide, T., Shearer, P. M., & Imanishi, K. (2014). Stress drop variations among small earthquakes before the 2011 Tohoku-oki, Japan, earthquake and implications for the main shock. *Journal of Geophysical Research: Solid Earth*, *119*, 7164–7174. https://doi.org/10.1002/2014JB010943

Vallée, M. (2013). Source time function properties indicate a strain drop independent of earthquake depth and magnitude. *Nature Communications*, *4*, 2606.

Vallée, M., Charléty, J., Ferreira, A. M., Delouis, B., & Vergoz, J. (2011). SCARDEC: A new technique for the rapid determination of seismic moment magnitude, focal mechanism and source time functions for large earthquakes using body-wave deconvolution. *Geophysical Journal International*, *184*(1), 338–358.

Vallée, M., & Douet, V. (2016). A new database of source time functions (STFS) extracted from the SCARDEC method. *Physics of the Earth and Planetary Interiors*, *257*, 149–157.

Vassiliou, M., & Kanamori, H. (1982). The energy release in earthquakes. *Bulletin of the Seismological Society of America*, *72*(2), 371–387.

Vernant, P., Reilinger, R., & McClusky, S. (2014). Geodetic evidence for low coupling on the hellenic subduction plate interface. *Earth and Planetary Science Letters*, *385*, 122–129.

Ye, L., Lay, T., Kanamori, H., & Rivera, L. (2016). Rupture characteristics of major and great ($M_w \geq 7.0$) megathrust earthquakes from 1990 to 2015: 1. Source parameter scaling relationships. *Journal of Geophysical Research: Solid Earth*, *121*, 845–863. https://doi.org/10.1002/2015JB012426

Yoneshima, S., Mochizuki, K., Araki, E., Hino, R., Shinohara, M., & Suyehiro, K. (2005). Subduction of the Woodlark Basin at New Britain Trench, Solomon Islands region. *Tectonophysics*, *397*(3), 225–239.

Zweck, C., Freymueller, J. T., & Cohen, S. C. (2001). Three-dimensional elastic dislocation modeling of the postseismic response to the 1964 Alaska earthquake. *Journal of Geophysical Research*, *107*(B4), 2002.